TÉCNICO LISBOA

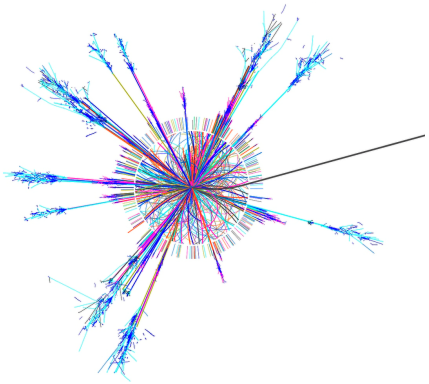

QGP effects on Energy Correlators inside jets

Marco António Coelho Leitão

Thesis to obtain the Master of Science Degree in

Engineering Physics

Supervisor: Prof. Dr. José Guilherme Teixeira de Almeida Milhano

Examination Committee

Chairperson: Prof. Dr. Mário João Martins Pimenta
Supervisor: Prof. Dr. José Guilherme Teixeira de Almeida Milhano
Member of the Committee: Prof. Dr. Liliana Marisa Cunha Apolinário

December 2023

To my parents and my sister.

Acknowledgments

First, I would like to thank my supervisor, Prof. Guilherme Milhano, for suggesting the topic of this thesis and for accepting to work with me. His constant availability and insights, mixed with great moments of humor, were crucial for the development of this work. I also thank him for reviewing this thesis and making relevant observations.

Next, I would like to thank my family, namely my parents and my sister. Their unconditional support for almost every crazy path I chose was more important than words can describe. If I have reached where I am, it's largely thanks to them.

Last, but not least, I want to thank all the colleagues and friends I have made throughout these years. All the hours spent discussing physics and, equally important, all the other fun moments were undoubtedly contributions to this thesis.

The work developed in this thesis was funded by FCT (Fundação Ciência e Tecnologia), under the scholarship CERN/FIS-PAR/0032/2021 "Bridging Theory and Experiment: Collider Phenomenology (II)"

Resumo

O estudo do plasma de Quarks e Gluões (QGP), a fase desconfinada da Cromodinâmica Quântica (QCD), constitui, atualmente, uma área de investigação muito ativa e em rápido desenvolvimento. O QGP é a fase do Universo no seu primeiro microssegundo de existência, podendo ser criado em colisões de iões pesados ultrarelativistas. Nessas experiências, jatos - sprays colimados de hadrões - podem ser formados, constituindo uma ferramenta crucial para estudar o QGP, feito por análise das suas modificações ao viajar pelo plasma através da comparação com jatos em colisões Protão-Protão, que evoluem no vácuo.

Uma das principais manifestações da interação dos jatos com o QGP é uma perda de energia significativa. Outra manifestação crucial é chamada de resposta do meio, constituindo um acréscimo de partículas decorrentes do QGP, que são reconstruídas dentro do jato final.

Neste trabalho, funções de correlação energia-energia, uma nova classe de observáveis, foram determinadas para jatos em colisões de iões pesados e analisadas. As funções de correlação evidenciaram as diferentes fases da QCD pelos quais os constituintes dos jatos passam, e a análise de modificações desprezando a resposta do meio apresentou um comportamento compatível com a ideia de que jatos que evoluem no QGP hadronizam a partir de uma escala de tempo posterior à de jatos que evoluem no vácuo. Essas funções de correlação também se mostraram sensíveis à resposta do meio, com sensibilidades diferentes considerando diferentes versões da função.

Palavras-chave: Cromodinâmica Quântica, Plasma de Quarks e Gluões, Jatos, Resposta do Meio, Funções de Correlação de Energia

Abstract

The study of the Quark-Gluon Plasma (QGP), the deconfined phase of Quantum Chromodynamics (QCD) matter, is a very active and fast-developing field of research. QGP is the phase matter of the Universe in its first microsecond of existence and can be created in collisions of ultra-relativistic Heavy-Ions. In such experiments, jets - collimated sprays of hadrons - can be formed, constituting a crucial tool to probe the QGP. This is achieved by studying their modifications when traveling through the QGP, by comparing with jets in Proton-Proton collisions, which evolve in the vacuum.

One of the main manifestations of the interaction of jets with the QGP (*jet quenching*) is a significative loss of energy. The other crucial manifestation is called medium response, constituting an addition of particles arising from the QGP that are reconstructed within the final jet.

In this work, energy correlators, constituting a novel class of observables, were computed for jets in Heavy-Ion collisions and analysed. These correlators are shown to imprint the different QCD phases that jets constituents go through, and the analysis of modifications neglecting medium response have presented a behaviour compatible with the idea that jets evolving in the QGP hadronize in a later timescale than jets evolving in the vacuum. These correlators have also shown to be sensitive to medium response, with distinct sensitivities considering different versions of the correlator.

Keywords: Quantum Chromodynamics, Quark-Gluon Plasma, Jet, Medium Response, Energy Correlator

Contents

List of Figures

Nomenclature

JEWEL Jet Evolution With Energy Losses

AA Nucleous-Nuclous

CFT Conformal Field Theory

CoM Center-of-Mass

EEC Energy-Energy Correlations

IRC Infrared and Collinear

LHC Large Hadron Collider

LO Leading Order

MC Monte Carlo

N^{i}LO (Next-to)^i Leading Order

PDF Parton Distribution Function

pp Proton-Proton

pQCD Perturbative Quantum Chromodynamics

QCD Quantum Chromodynamics

QFT Quantum Field Theory

QGP Quark Gluon Plasma

SM Standard Model

UHRIC Ultra Relativistic Heavy-Ion Collisions

Chapter 1

Introduction

This chapter aims to develop the main building blocks of this work, beginning by introducing the core theories behind it: the Standard Model (SM) and, in particular, its sector Quantum Chromodynamics (QCD). We then proceed by outlining the main characteristics of QCD, further exploring their consequences in phenomenology. The chapter closes with an outline of this thesis.

1.1 The Standard Model of Particle Physics

The Standard Model (SM) of Particle Physics [1–3] is currently the most successful Quantum Field Theory (QFT) describing three of the four known fundamental interactions: the *electromagnetic*, the *weak* and the *strong* forces. It corresponds to an SU(3) × SU(2) × U(1) gauge theory [4, 5], governed by four classes of field particles: Quarks, Leptons - both also referred to as *fermions* (spin-1/2 particles) -, Gauge Bosons (spin-1 particles, mediators of the different interactions) and the Higgs Boson. In this section, we aim to briefly describe every class and their respective roles in the theory.

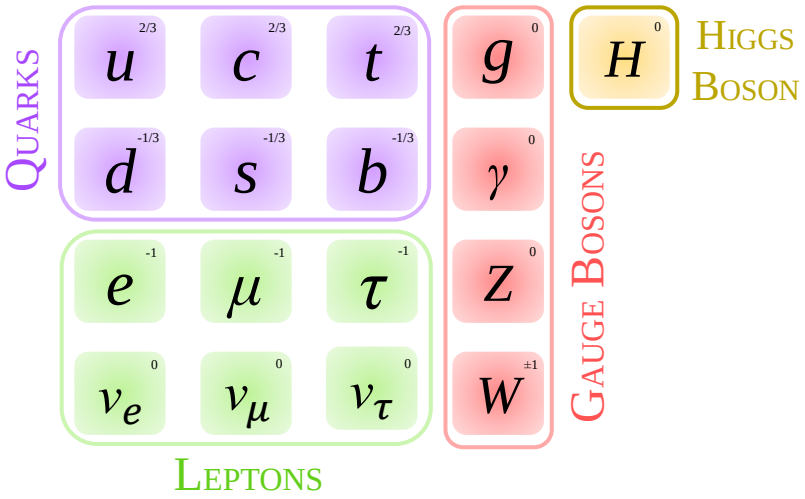

Figure 1.1: The particles constituting the Standard Model, divided in Quarks, Leptons, Gauge Bosons and the Higgs Boson. The charge for each particle is indicated on the superior left corner, in units of the elementary charge.

Figure 1.1 displays the SM's constituting particles. This theory distinguishes six different flavors of quarks (*u*p, *d*own, *c*harm, *s*trange, *t*op, *b*ottom) and six different flavors of leptons (electron, e, muon, μ, tau, τ, and respective neutrinos). Quarks in the first row (up, charm, top) have a charge of 2/3, in terms of elementary charge, while those in the second row (down, strange, bottom) carry a charge of $-1/3$. On the lepton sector, the first row particles (e, μ, τ) are endowed with a charge of -1 and the corresponding neutrinos are chargeless. For each one of these fermions, there exists an anti-fermion, with opposite charge.

Gauge bosons are fundamental components of the SM's structure, as each mediates a class of interactions. The eight gluons, g_i, govern the strong interaction between quarks and gluons themselves, and are associated with the SU(3) symmetry. The weak and electromagnetic forces are unified in the *electroweak* interaction, associated with the SU(2) $\times$ U(1) symmetry. This unification gives rise to the photon, γ, responsible for the electromagnetic force exclusive to electrically charged particles, as well as the bosons $W^{\pm}$ and Z, both mediators of the weak interaction between fermions.

Finally, we arrive at the Higgs boson. The existence of this particle is crucial for the SM; it explains the mass of most particles in the theory. In essence, the Higgs boson is a result of incorporating the *Higgs mechanism* [6–9] into the SM, achieved by initially adding a scalar field doublet in the theory. The *spontaneous symmetry breaking* (SSB) gives mass directly to the $W^{\pm}$ and Z bosons[1], while the quarks and charged leptons' masses are a result of a transformation on the Yukawa interactions terms, which were a consequence of adding the scalar field.

The Higgs boson was discovered in 2012, at the LHC [10], establishing the SM as one of the most successful fundamental theories ever built. However, it is still not complete, as it fails to explain the mass of the neutrinos, which are massless in this framework, does not account for gravity, and does not incorporate dark matter and energy. Many extensions and alternate theories have been proposed throughout the years [11], but none has yet been experimentally confirmed. For the purpose of this thesis, the referred limitations are not relevant, and the SM will be used as our most general framework.

1.2 Quantum Chromodynamics

1.2.1 Classical Lagrangian

Quantum Chromodynamics (QCD) is the sector of the SM ruling the dynamics of quarks and gluons via strong interaction [12]. It is an SU(3) non-abelian Gauge Theory, described by the Lagrangian

$$\mathcal{L}_{\text{QCD}} = -\frac{1}{4} F_a^{\mu\nu} F^a_{\mu\nu} + \bar{\psi}(i\not{D} - M)\psi, \tag{1.1}$$

where ψ represents the quark/anti-quark fields, each transforming under the fundamental representation of SU(3), and $F_a^{\mu\nu}$ the field-strength tensors, given by

$$F_a^{\mu\nu} = \partial^\mu A_a^\nu - \partial^\nu A_a^\mu + g_s f_{abc} A_b^\mu A_c^\nu, \quad (a = 1, ..., 8) \tag{1.2}$$

[1] The Goldstone modes originated from SSB are absorbed the by these bosons

responsible for the dynamics and self-interaction of the eight gluons A^a_μ, which in turn transform under the adjoint representation of SU(3). The covariant derivative,

$$D_\mu = \partial_\mu - ig_s T_a A^a_\mu, \tag{1.3}$$

produces the kinetic terms for the quarks, as well as interactions with gluons, allowing the Lagrangian to be Gauge Invariant. The constants f_{abc} and g_s are, respectively, the structure constants of the adjoint representation of SU(3) and the coupling constant of QCD, while T_a correspond to the generators of the SU(3) Lie Algebra.

Quarks and gluons, collectively referred to as *partons*, admit an extra degree of freedom due to their transformation properties under SU(3) actions, named *color*. Quark (anti-quark) fields may possess one of three colors (anti-colors): r ($\bar{r}$), g ($\bar{g}$) and b ($\bar{b}$), while gluons may possess eight. Color is the conserved charge in the strong interaction, hence only quarks and gluons are allowed participate in these interactions.

In nature, free colored particles are never observed - quarks, for instance, are always confined into colorless (i.e. SU(3) singlets) hadrons, such as protons (uud[2]) and neutrons (udd). This is phenomena is known as *color confinement*, and while it is experimentally well established, it is not fully understood how it dynamically happens, constituting one of the most important open questions in QCD.

1.2.2 Running Coupling

QCD is a renormalizable theory. As a result, we can write a Renormalization Group Equation (RGE), which will rule the evolution of the coupling constant g with a momentum scale μ. The RGE takes the form

$$\mu \frac{\mathrm{d}g}{\mathrm{d}\mu} = \beta(g), \tag{1.4}$$

where $\beta(g)$ is a function of the coupling constant, called Beta function, encoding the behavior of the running coupling with the momentum scale.

The computation of the QCD Beta function, subject of a Nobel Prize award in 2004 to Gross, Politzer and Wilczek [13–15], is quite an extensive and technical calculation, involving the renormalization of some vertices, which is beyond the scope of this work. Here, we merely state the result, at one-loop order, or *next-to-leading-order* (NLO):

$$\beta(g_s) = -b_0 g_s^3 + \mathcal{O}(g_s^5), \tag{1.5}$$

with $b_0 = \frac{1}{(4\pi)^2}\left(11 - \frac{2}{3}N_f\right)$, where N_f is the number of quark flavours. Inserting in Eq. (1.4), one obtains

$$g_s^2(\mu) = \frac{g_s^2(\mu_0)}{\frac{b_0 g_s^2(\mu_0)}{2}\ln\frac{\mu}{\mu_0} + 1}, \tag{1.6}$$

where μ_0 is a reference scale. Equivalently, using $\alpha_s = \frac{g_s^2}{4\pi}$, $\beta_0 = (4\pi)^2 b_0$ and defining Λ_{QCD} as the

[2] This reads "bound state of two quarks up and one quark down".

scale for which the denominator becomes zero (at NLO; for higher orders, it is the pole of the coupling constant), we arrive at

$$\alpha_s(\mu) = \frac{1}{\frac{\beta_0}{4\pi} \ln \frac{\mu^2}{\Lambda^2_{\text{QCD}}}}. \tag{1.7}$$

In scattering processes, the scale μ is usually associated with the momentum transfer between particles involved, commonly denoted by Q.

The value of Λ_{QCD} can be determined by knowing the value of the coupling constant at a given reference scale, for instance M_Z^2 (M_Z mass of the Z boson) [16], and depends on the order of perturbation theory, number of flavors involved and the renormalization scheme. In Figure 1.2, theoretical predictions at fourth-loop other is displayed alongside experimental values, for $\alpha(M_Z^2) = 0.1179 \pm 0.0010$.

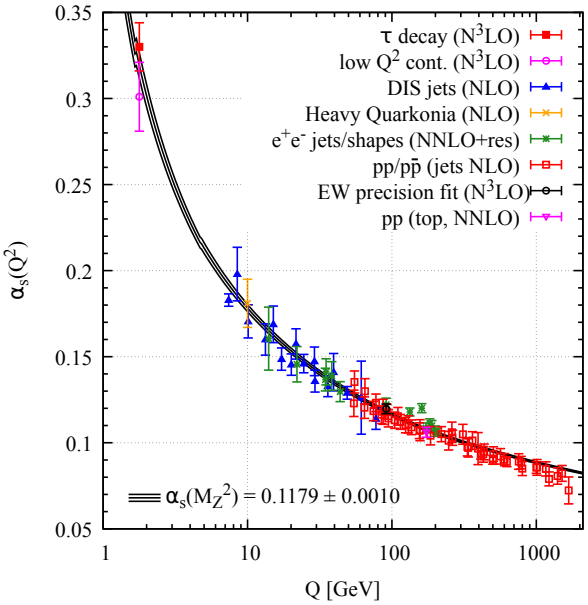

Figure 1.2: Running coupling of QCD, with the triple line corresponding to the theoretical prediction at fourth-loop order and the points corresponding to experimental results. Taken from PDG data [16].

Λ_{QCD} is the scale where perturbation theory breaks. For close momentum scales $\mu \gtrsim \Lambda_{\text{QCD}}$ or bellow, the coupling constant becomes of $\mathcal{O}(1)$, entering the non-perturbative regime, where most theoretical predictions based in perturbative QCD (pQCD) are no longer valid (such as Eq. (1.7)). As a consequence, the theory is strongly interacting, and the partons will inevitably confine in bound states. This is compatible with color confinement; partons always confine in colorless hadrons. On the filp-side, for higher scales, the theory is weakly coupled, and the higher the momentum scale involved, the less quarks and gluons couple to each other, resulting in *asymptotic freedom*.

1.2.3 QCD Phase Diagram

The theory's distinguished characteristics at different momentum scales yields some remarkable behaviors of QCD matter. This is described by the *QCD phase diagram* [17], sketched in Figure 1.3, displaying the different phases of QCD matter at different temperatures and net baryon density (excess of quarks

over anti-quarks). In this work, we'll be mainly interested in probing the state of matter related to the

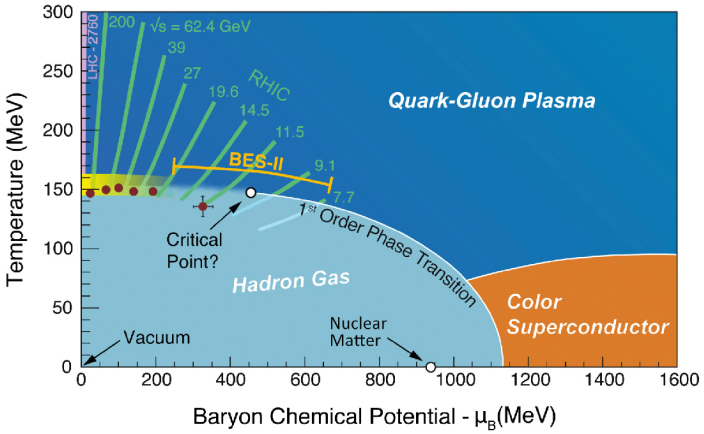

Figure 1.3: QCD Phase Diagram. Different phases of QCD matter are displayed in terms of Temperature, in MeV, and Net Baryon Density. Taken from [18].

high-temperature, dense and deconfined region of this diagram, usually referred to as the Quark-Gluon Plasma (QGP).

The QCD phase diagram highlights a smooth transition between confined hadrons and deconfined quark-gluon phase, at high temperatures and low net baryon density. This motivates the study of ultra-relativistic Heavy-Ion collisions, where the extreme conditions required for this transition and the formation of the QGP can be achieved. We will turn back on the heavy-ion collisions in section 1.3.3, in the wake of discussing QCD processes, where the phenomenology of such collisions and the evolution of the QGP will be described. Before moving on, in the next section, some key results and concepts in QCD, also necessary in order to build up towards that discussion, will to be presented.

1.2.4 Parton branching and IRC divergences

Let us consider a process with matrix element $\mathcal{M}_h^{(n)}$, where one of the outcome particles is a quark with momentum p. The quark then emits a soft and collinear gluon, with $k \ll q$, as pictured in Figure 1.4, with an angle $\theta \ll 1$ in the center of mass relative to the quark momentum's direction.

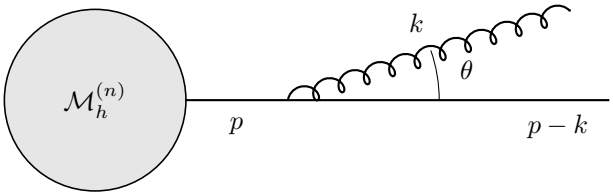

Figure 1.4: Diagramatic representation of a gluon emission from a quark.

Analogously to what was done in [12], the differential cross-section of this whole process, $\mathrm{d}\sigma^{(n+1)}$, is found to be given by, in the massless and soft limit,

$$\mathrm{d}\sigma^{(n+1)} = \mathrm{d}\sigma^{(n)} \times \mathrm{d}S, \tag{1.8}$$

where $\mathrm{d}\sigma^{(n)}$ is the differential cross-section of the process without emission and $\mathrm{d}S$ is the gluon's emission

probability, given by

$$\mathrm{d}S = \frac{\alpha_s C_F}{\pi} \frac{\mathrm{d}E_k}{E_k} \frac{\mathrm{d}\theta^2}{\theta^2}. \tag{1.9}$$

This quantity features two remarkable divergences: the limits $\theta \to 0$ (collinear divergence) and $E_k \to 0$ (infrared divergence), both belonging to the class of *logarithmic divergences*, given that $\mathrm{d}x/x = \mathrm{d}\log(x)$. In this particular case, the divergence is completely removable at every order in perturbation theory, when considering, for instance, the virtual diagrams (in this case, this is also guaranteed by the KLN theorem). However, for some observables, these divergences may not be removable.

Observables where both collinear and infrared divergences can be removed are named *Infrared and Collinear* (IRC) *safe*, and constitute the most desirable observables to work with in QCD. IRC safe observables allow to safely use perturbation expansions in pQCD, which are important for phenomenological calculations and also compatible with experiment.

A generalization of Eq. (1.9) to a collinear parton branching $a \to b + c$, where the daughter parton c has a fraction of momentum $z \ll 1$ of the parent parton a (is the "emitted" one), at NLO, is given by

$$\mathrm{d}\mathcal{S} = \frac{\alpha_s C_f}{\pi} \hat{P}^{(0)}_{bc \leftarrow a}(z) \mathrm{d}z \frac{\mathrm{d}Q^2}{Q^2}, \tag{1.10}$$

where $\hat{P}_{i \leftarrow j}(z)$ are the unregularized splitting kernels, which describe the natural probability of a parton a to split into $b + c$ and are given, at LO, by

$$\begin{aligned}
\hat{P}^{(0)}_{g \leftarrow q}(z) &= C_F \frac{1 + (1-z)^2}{z}, \\
\hat{P}^{(0)}_{g \leftarrow g}(z) &= 2C_A \left[\frac{z}{1-z} + \frac{1-z}{z} + z(1-z) \right], \\
\hat{P}^{(0)}_{q \leftarrow g}(z) &= T_F \left(z^2 + (1-z)^2 \right), \\
\hat{P}^{(0)}_{q \leftarrow q}(z) &= C_F \left[\frac{1+z^2}{1-z} \right],
\end{aligned} \tag{1.11}$$

with $C_A = 3$, $T_F = 1/2$ and $C_F = 4/3$ for $N_c = 3$ QCD colors. Parton branching is a key concept, given that most scattering processes in QCD undergo this phenomenon. The most important scattering experiments in the context of this theory, and also of this work, will be readily outlined and discussed.

1.3 Proton-Proton and Heavy-Ion collisions

Due to confinement, one can never directly collide quarks. Experimental scattering processes of interest, where QCD phenomena may take place, are either hard e^+e^- annihilations or collisions involving hadrons, such as Deep Inelastic Scattering (DIS), corresponding to the scattering of an electron with a proton, Proton-Proton (pp) and Heavy-Ion (AA) collisions. In this section, we aim to explore the phenomenology of Proton-Proton and Heavy-Ion collisions.

It is important to note that in hard scattering processes, such as the ones we have just enumerated, quarks and gluons usually undergo from asymptotically free colored partons, which is governed by perturbation theory, to hadrons, in turn non-perturbative structures, constituting the final particles that are

detected in experiment. The *hadronization process* (i.e. the process where hadrons form from nearly free partons) cannot, therefore, be described using the usual techniques of perturbation theory. This increases the complexity in describing QCD processes, requiring the development of techniques and models in order to properly analyze these processes, such as effective hadronization models, factorization techniques that allow to separate perturbative calculations from non-perturbative structures (subject of subsection 1.3.1) and the study of final-state objects and observables that reduce hadronization dependence. Examples of such objects are *jets*, which will be introduced in section 1.3.2 in the context of Proton-Proton collisions.

1.3.1 Parton Distribution and Fragmentation Functions

Hadronic compositions in the initial or final state of a process can become a problem, given that perturbative calculations are only valid at a parton level and hadrons constitute complex systems of partons with a non-perturbative nature. However, in many hard processes of interest, such as pp collisions, it is possible to (approximately) separate perturbative calculations from the hadronic structures using a factorization theorem, which roughly states that the cross-section of the hard process is assumed to take the form of a convolution between functions encoding the structure of the colliding hadrons, named *parton distribution functions* (PDFs), the perturbative partonic cross-section and, if appliable, a function encoding the fragmentation of partons into final-state hadrons, the *fragmentation functions* (FFs).

PDFs and FFs are phenomenological (and non-perturbative) objects that can only be determined by a wide-range of experimental data. PDFs, on the one hand, are built in analogy with form factors for Rutherford-like experiments; in the context of hard protonic processes, one defines a PDF, $f_i^H(x, \mu^2)$, as the probability density of finding the constituting quark i with a fraction x of the total momentum of the hadron H, at a given resolution scale μ^2, which is analogous to a renormalization scale. On the other hand, the FFs, denoted $D_h^k(x_h, \mu^2)$, stand for the probability density of a parton k fragmenting into an hadron h with a fraction x_h of its momentum. For both quantities, in a hard scattering, the resolution scale μ has the role of regulating the transition between peturbative and non-perturbative QCD, and are usually taken as the momentum transfer in the process.

Even though PDFs and FFs constitute non-perturbative objects, their evolution with the scale μ is perturbative, described by the Dokshitzer-Gribov-Lipatov-Altarelli-Parisi (DGLAP) equations. For instance, in the case of FFs, the DGALP equations take the form

$$\frac{\partial D_h^i(x_h, \mu^2)}{\partial \ln \mu^2} = \frac{\alpha_s(\mu^2)}{2\pi} \sum_j \int_{x_h}^1 \frac{\mathrm{d}z}{z} P_{j\leftarrow i}(z)\, D_h^j\left(\frac{x_h}{z}, \mu^2\right), \tag{1.12}$$

where $P_{j\leftarrow i}$ are the *regularized* splitting kernels, which can be obtained from the unregularized kernels in Eq. (1.11) through

$$\int_x^1 \mathrm{d}z P_{i\leftarrow j}(z) f(z) = \int_x^1 \mathrm{d}z \hat{P}_{i\leftarrow j}(z) f(z) - \int_0^1 \mathrm{d}z \hat{P}_{i\leftarrow j}(z) f(1), \tag{1.13}$$

yielding

$$
\begin{aligned}
P_{g\leftarrow q}(z) &= C_F \frac{1+(1-z)^2}{z}, \\
P_{g\leftarrow g}(z) &= 2C_A \left[\frac{z}{(1-z)_+} + \frac{1-z}{z} + z(1-z) + \left(\frac{11}{12} - \frac{N_f T_F}{3C_A}\delta(1-z) \right) \right], \\
P_{q\leftarrow g}(z) &= T_F \left(z^2 + (1-z)^2 \right), \\
P_{q\leftarrow q}(z) &= C_F \left[\frac{1+z^2}{(1-z)_+} + \frac{3}{2}\delta(1-z) \right].
\end{aligned}
\tag{1.14}
$$

Here, we are using the "+" superscription, arising from the regularization process described in Eq. (1.13), being implicitly defined by

$$
\int_0^1 \mathrm{d}z f(z)_+ \; g(z) \overset{\text{idef}}{=} \int_0^1 \mathrm{d}z f(z)(g(z) - g(1)). \tag{1.15}
$$

The evolution of the fragmentation functions with splitting kernels provides a picture of parton evolution through a sequence of $1 \to 2$ splittings. As a result, partons participating in a hard scattering are expected to undergo a *parton showering*, proceeded by the hadronization process, as sketched in Figure 1.5. Hence, in this interpretation, FFs can be roughly thought as the functions encoding the showering and hadronization of a given parton in a given process.

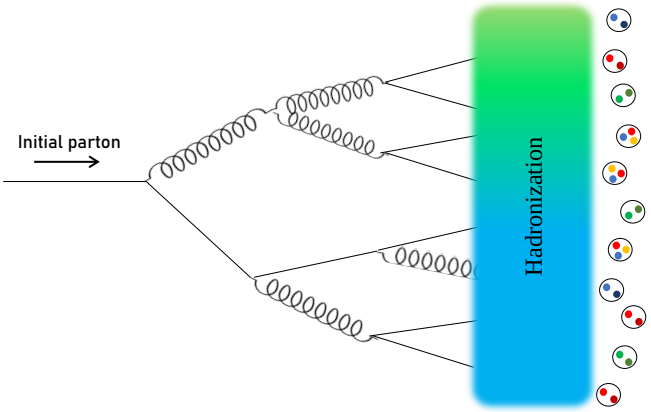

Figure 1.5: Sketch of a parton showering and subsequent hadronization (time flows from left to right).

1.3.2 Proton-Proton Collisions

It is clear that PDFs and FFs constitute essential ingredients in any collision experiment involving hard protons and final hadronic states. In the case of pp collisions [19], the cross-section involving at least one hadronic composition h in the final state can be factorized according to

$$
\begin{aligned}
\sigma(\mathrm{pp} \to h + X) &= \sum_{i,j,k} f_i^{\mathrm{p}} \otimes f_j^{\mathrm{p}} \otimes \sigma(i+j \to k) \otimes D_h^k \\
&= \sum_{i,j,k} \int_0^1 \mathrm{d}x_i \int_0^1 \mathrm{d}x_j \int_0^1 \mathrm{d}x_h f_i^{\mathrm{p}}(x_i,\mu^2) f_j^{\mathrm{p}}(x_j,\mu^2)\; \sigma(i+j \to k; x_i, x_j, \mu^2) D_h^k(x_h,\mu^2),
\end{aligned}
\tag{1.16}
$$

where the sum in i, j and k is being performed over all participating partons, with i and j being related to the colliding protons and k to the hadron h. The total cross-section does not depend on the factorization scale, given that the scale dependence of the PDFs and FFs are compensated by the cross-section of the perturbative process $i + j \to k$ due to the DGLAP equations.

Different bunches of particles and compositions can come in a final state of hard pp collisions. Our interest relies on the cases where a scattering of two partons with a high momentum component perpendicular to the boost direction (the *transverse component*, p_T) occurs, which leads to the formation of collimated sprays of hadrons or, in other words, a narrow cone of high-p_T hadrons, present in the final state. These objects are named *jets*, constituting a proxy of the initial interacting hard partons, also containing information on the showering and hadronization process their constituents went through.

In pp collisions, these hard scatterings can occur in a way that leads, for instance (and most importantly in the context of this work), to the formation of two jets (a dijet event), a Z-boson and a jet (Z+jet event) and a γ and a jet (a γ+jet event). The process we have just described above is schematized in Figure 1.6, where for the sake of representation we display in the final state a Z+jet.

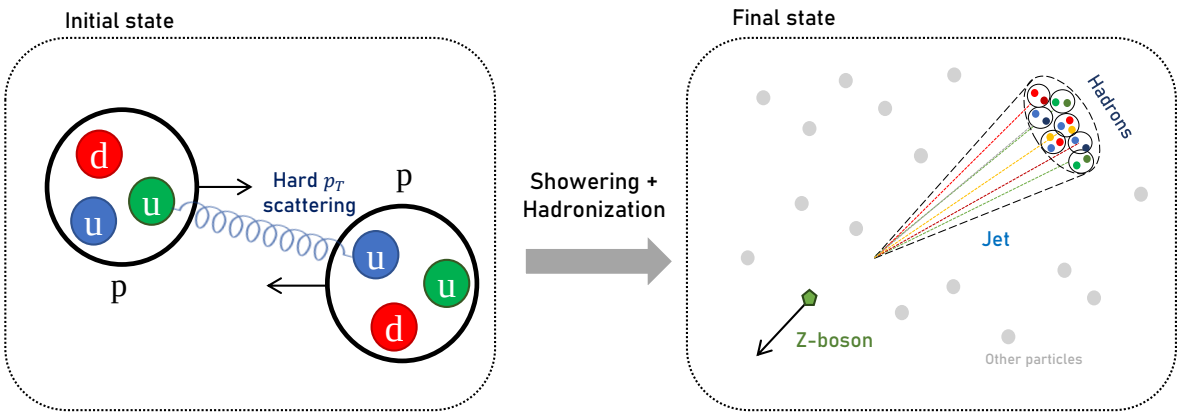

Figure 1.6: Formation of jets schematized. For the sake of representation, the final state displays the Z+jet outcome.

Due to the transverse "nature" of jets, and the fact that the center of mass of the colliding system is boosted in the longitudinal direction (and is unknown), it is desirable to introduce more suitable and robust kinematic variables in the transverse plane, perpendicular to the boost. Taking the z direction as the longitudinal boost and $p^\mu = (E, p_x, p_y, p_z)$, we naturally define the transverse momentum vector as $\vec{\boldsymbol{p}}_T = (p_x, p_y)$ in the transverse plane (x, y), with its modulus given and denoted by

$$p_T \stackrel{\text{def}}{=} \sqrt{p_x^2 + p_y^2}. \tag{1.17}$$

We also define the transverse mass,

$$m_T \stackrel{\text{def}}{=} \sqrt{p_T^2 + m^2} - p_T, \tag{1.18}$$

and the rapidity,

$$y \stackrel{\text{def}}{=} \frac{1}{2} \log\left(\frac{E + p_z}{E - p_z}\right), \tag{1.19}$$

allowing to express the four-momentum of a particle as

$$p^\mu = ((m_T + p_T)\cosh(y), p_T\cos(\phi), p_T\sin(\phi), (m_T + p_T)\sinh(y))\,, \tag{1.20}$$

where ϕ is the azimuthal angle. These introduced variables are the closest one can get to the traditional conserved quantities in non-longitudinal boosted collisions; for instance, a difference $y_1 - y_2$ in rapidity is boost-invariant. We finally define a pairwise distance on the (y, ϕ) plane,

$$\Delta R_{ij} \overset{\text{def}}{=} \sqrt{(y_j - y_i)^2 + (\phi_j - \phi_i)^2}. \tag{1.21}$$

1.3.3 Heavy-Ion Collisions and the formation of the Quark Gluon Plasma

In this section, we will breifely describe the phenomenology behind the other class of scattering experiments of interest, the Ultra-Relativistic Heavy-Ions Collisions, usually Pb or Au nuclei, also denoted AA collisions and abbreviated as URHIC [20].

In URHICs, the massive colliding nuclei are highly contracted on the boost's direction, therefore constituting very thin disks and complex "seas" of partons. When these systems collide, many soft interactions take place, where there is the exchange of some color charge, creating longitudinal color fields that fill the space between the colliding systems. This yields an increase of the energy densities and temperature at the collision center to very extreme conditions, shortly after the collision, leading to the formation of a QCD matter droplet of very high density, strongly coupled and of nearly free partons: the Quark Gluon Plasma, QGP.

At the initial stage of QGP's formation and evolution, as sketched in Figure 1.7, the medium's region at the colliding center undergoes a pre-equilibrium phase (Pre-QGP) till it thermalizes. The QGP subsequently lives for a short period of time (about $\sim$ 10 fm/c), cooling down to a scale where the hadronization of the previously deconfined partons start taking place - a mixed phase, proceeded by the complete formation of a hot hadron gas. Finally, the system freezes out, and only free hadrons are left.

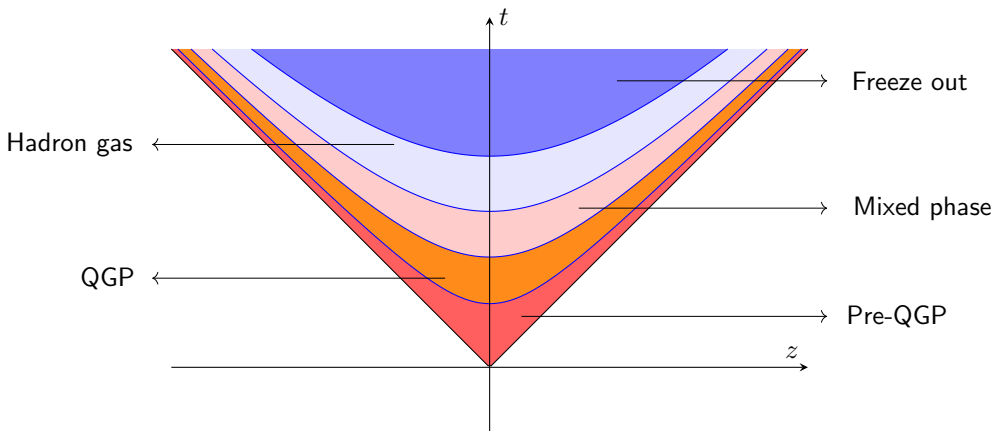

Figure 1.7: QGP evoultion sketched in a space-time diagram.

This deconfined, extreme phase of QCD matter, first discovered through studies of URHICs of Au + Au at the Relativistic Heavy Ion Collider (RHIC) and later confirmed at the Large Hadron Collider

(LHC) [21], has been raising interest in both theorists and experimentalists over the past decades, given that it is believed to be the state of the Universe within ~ 1 μs after the Big-Bang. This clearly motivates the creation of tools that probe the QGP, one of which will be introduced right away.

1.3.4 The common denominator (Probing the QGP)

In the context of URHICs, what happens when two hard incident partons scatter off? The answer is similar to the case of pp collisions: the formation of jets. Jets constitute, hence, a "common denominator" between URHICs and pp collisions, being one of the main reasons why these processes are often studied together. The key difference between jets in URHICs and pp collisions, making these studies so important in QCD phenomenology, lies on the observation that, in the first, the jet evolving particles will travel through the QGP droplet, giving rise to modifications of their kinematic properties and structures due to interactions with the medium. In contrast, in pp collisions, jets evolve in vacuum.

Studying modifications of jets due to their evolution in the medium, which can be achieved by comparing URHIC's jets to those from pp collisions, may teach us about the internal working of the QGP. This is the closest route to probe the QGP using scattering experiments, which are known to have brought great developments in modern physics, such as the discovery of the atomic nucleus by Rutherford [22] and the discovery of quarks within protons [23]. Many analysis methods to identify and study the internal properties of jets in collider experiments have been developed throughout the past decades, some of which will be outlined in section 1.5. The application and the established effects on jets by the presence of QGP will be explored in chapter 2.

1.4 Monte Carlo Parton Showers

In the wake of the discussions on some QCD processes, we will now present an important result that allows for a probabilistic sampling of a parton shower. The natural way to picture this approach is by analysing the probability of emission within an interval of the momentum scale. However, calculations become more convenient by analysing the probability of no emission instead.

The probability of no emission to occur up to a scale $Q^2 + \mathrm{d}Q^2$ is given by the probability of no emission up to a scale Q^2 multiplied by the probability of no emission in the interval $[Q^2, Q^2 + \mathrm{d}Q^2]$, in turn determined by the complementary of the probability in Eq. (1.10), integrated in a range of z where the splittings are defined to be resolved (i.e. within a given scale-dependent cut-off in order to avoid divergences) and summed over all possible partons b. In equation form,

$$\Delta(Q^2 + \mathrm{d}Q^2) = \Delta(Q^2)\left(1 - \int_z \frac{\alpha_s C_f}{\pi} \sum_b \hat{P}^{(0)}_{b\leftarrow a}(z)\mathrm{d}z \frac{\mathrm{d}Q^2}{Q^2}\right). \tag{1.22}$$

Performing successive continuous iterations, from Q_0 to Q, the probability of no parton emission between

$[Q_0, Q]$ is found to be

$$\Delta([Q_0^2, Q^2]) = \exp\left(-\int_{Q_0^2}^{Q^2}\int_z \frac{\alpha_s C_f}{\pi}\sum_b \hat{P}^{(0)}_{b\leftarrow a}(z)\mathrm{d}z\frac{\mathrm{d}Q^2}{Q^2}\right). \tag{1.23}$$

This is the *Sudakov Form Factor*, constituting the basis of parton showers, as implemented in Monte Carlo generators such as PYTHIA [24]. We will briefly describe the internal workings of a (simplified) parton shower.

Let's consider the i'th step of a branching tree, with scale Q_i^2. The decision whether a further splitting will occur is determined by generating a random number r from a uniform distribution in $[0, 1]$. If the Sudakov factor $\Delta([Q_{i-1}^2, Q_i^2])$ lies below this number, no further branching step is generated from here, and the parton will constitute a final parton ready for hadronization. Otherwise, the branching will continue, and the splitting fraction z_i can be obtained by sampling within the allowed z range with probability proportional to $\hat{P}^{(0)}_{b\leftarrow a}(z)$. This iteration proceeds until one reaches a scale Q_i bellow a cuttoff scale Q_0.

1.5 Jet definitions and algorithms

The previous discussion on URHICs and pp collisions made the necessity for developing methods to analyse jets in collider experiments quite clear. In this section, we aim to lay out the main techniques for identifying jets.

Experimentally (and in computational simulations), the outcome of collisions is usually presented as a set of final-state particles (e.g. hadrons), each in the form of 4-momentum vectors. These sets will be referred to as *events*. The first task in jet studies is naturally to identify jets given a certain event, which can be achieved via *jets algorithms*, i.e., sets of rules with parameters dictating how particles are clustered allied with a *recombination scheme*, used to obtain the jet's kinematic properties from its constituents. The most widely used recombination scheme is the *E-scheme*, where the jet momentum is obtained by the sum of all its constituents' momenta. The combination of a jet algorithm (with its parameters specified) and a recombination scheme is called a *jet definition*.

Jet algorithms are usually classified as *sequential recombination* or *cone* algorithms [25]. Sequential recombination algorithms are based on the previously discussed ideas that jets are products of successive parton branches, and so the clustering is done essentially by inverting the process, successively recombining two particles into one. In cone algorithms, jets are interpreted as dominant flows of energy, suggesting that we can reconstruct jets by defining a cone in the transverse plane to the beam direction and search for particles within this cone. Given its advanced development and the existence of highly efficient libraries (e.g. `FastJet` [26]), sequential recombination algorithms are usually preferred, and we will be using these throughout the entirety of this work.

Most sequential recombination algorithms of interest constitute a particular case of the "Generalized k_t-algorithm". For these algorithms, given a list of particles (i.e. a list of 4-momentum vectors), we firstly

define an *inter-particle* distance d_{ij} and a *beam* distance d_{iB} as follows:

$$d_{ij} \overset{\text{def}}{=} \min\left(p_{T,i}^{2p}, p_{T,j}^{2p}\right)\left(\frac{\Delta R_{ij}}{R}\right)^2, \tag{1.24}$$

$$d_{iB} \overset{\text{def}}{=} p_{T,i}^{2p}, \tag{1.25}$$

where p and R are free parameters, the latter usually denoted by jet radius, and ΔR_{ij} is the geometric distance as defined in Eq. (1.21). Then, at each iteration, the distances d_{ij} are computed for all pairs (i, j) and d_{iB} for all objects i, further proceeding according to the following conditions:

- if the smallest distance is a d_{ij}, objects i and j are clustered into a new object k, using the recombination scheme to find its kinematic properties. i and j are removed from the list and k is added;
- otherwise, if the smallest distance is a d_{iB}, i is identified as a jet and removed from the list.

These iterations continue until no more particles are left in the list. As a result, we obtain another list of objects, now identified as jets, and the clustering history.

Different specific values of the parameter p give particular the cases of this algorithm, such as the k_T-algorithm ($p = 1$), the C/A algorithm ($p = 0$) and the anti-k_T algorithm ($p = -1$). Jets that are reconstructed by different procedures are different jets, even if the constituents are the same, given that the clustering history, which can be physically interpreted as the jet's showering sequence, is generally not. The phase space for C/A and Anti-k_T jets are represented in Figure 1.8.

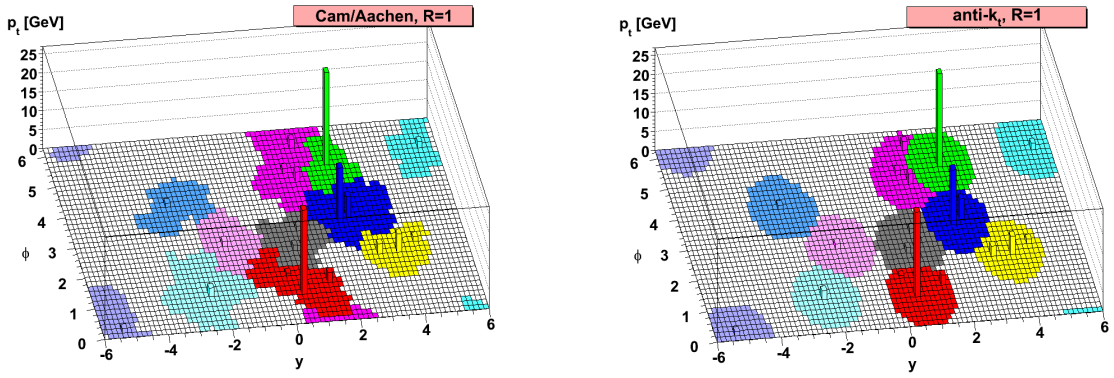

Figure 1.8: Phase space of C/A (right) and Anti-k_T (left) jets sketched. Shaded regions represent the clustering region of each jet, with a reconstruction radius R = 1. Taken from [27].

For the C/A algorithm, the clustering is done considering only the distances between the particles, beginning by joining the closest particles first; no momenta are considered, and the final jets are purely geometrical. On the other hand, the anti-k_T algorithm clustering takes preference on particles with higher transverse momentum, such as those constituting high-energy jets, being less sensitive to the existence of soft particles. Anti-k_T jets are shown to possess more regular contours and are preferred in experiment. This should not, however, diminish the importance of the other algorithms like the C/A algorithm, which is used for instance, to study the internal and kinematic properties of jet through jet substructure methods [28].

1.6 Thesis Outline

Given this generic introduction to QCD and Jet physics, we are in a position to develop the main arguments of this thesis. The next chapters are organized as follows.

In Chapter 2, we enumerate and discuss the main effects of the QGP medium on jets, evidenced with experimental and computational results. Then, the structure and implementation details of the main event generators to be used throughout this work are outlined.

The observables to be studied in this work - Energy Correlators - are introduced and explained in Chapter 3.

Chapter 4 acts as a preparation to the subsequent chapters, by outlining the main computational technicalities set to produce the results.

In Chapter 5 and 6, we aim to analyse the impact of the modifications discussed in Chapter 2 in energy correlators, through results obtained in computational simulations, constituting the main and original results of this work.

Finally, the conclusions of this work are drawn in Chapter 7.

Chapter 2

Jets in Heavy-Ion Collisions

So far, jets have been discussed in very general terms. We will now turn our attention towards jets in heavy-ion collisions, where the presence of the QGP droplet must be considered.

In this chapter, we shall qualitatively explore the known and predicted manifestations of the interactions between jets and the QGP. Later on, the two heavy-ion event generators used in the context of this work, JEWEL and HYBRID, will be described.

2.1 Energy Loss

Modification of jets in URHICs arise from the transfer of color and momentum between jet particles and the QGP medium. However, such interactions may present different manifestations.

The main and most experimentally well-established [29] manifestation is the loss of the total energy and momentum of a jet after traveling through the QGP medium, which is also commonly referred to as *jet quenching*. This energy loss is usually of $\mathcal{O}(10\text{ GeV})$ per jet, which is a huge amount of energy, given that jets lose this in a span of only a few fm of distance. This constitutes the first real evidence that matter produced in URHICs is strongly coupled.

To quantify these energy losses, the most commonly used observable is the *nuclear modification factor*, R_{AA}, defined by

$$R_{\mathrm{AA}}(p_T) \overset{\mathrm{def}}{=} \frac{\mathrm{d}\sigma^{\mathrm{AA}}/\mathrm{d}p_T}{\langle N_{\mathrm{coll}}\rangle \mathrm{d}\sigma^{\mathrm{pp}}/\mathrm{d}p_T}, \tag{2.1}$$

where $\mathrm{d}\sigma^{\mathrm{xx}}/\mathrm{d}p_T$ is the cross-section for producing jets in xx-collisions (AA or pp), and $\langle N_{\mathrm{coll}}\rangle$ is the equivalent number of pp collisions, per transverse momentum p_T, occurring in a heavy-ion collision. The R_{AA} compares the number of jets produced in AA collision with the expected number of jets produced in an equivalent number of pp collisions, without the presence of QGP, for a given value of p_T. The energy loss produces a (non-uniform) shift on the jet p_T spectrum, which in turn is very steep ($\sim p_T^{-6}$), resulting on the R_{AA} being a very sensitive measure.

The R_{AA} can also be computed for objects other than jets, such as bosons, in particular photons or a $Z-$bosons. This is quite important, given that these bosons do not participate in strong interactions and can't interact with the QGP. Thus, their R_{AA} is expected to be 1, constituting a useful benchmark

to our analysis procedures.

Fig. 2.1 displays the jet p_T spectrum, on the left, and results for the R_{AA} on the right, using simulated data from JEWEL, for jets and Z-bosons in Z+jet events. Given that JEWEL only simulates nucleon+nucleon collisions, $\langle N_{\mathrm{coll}} \rangle = 1$, and the R_{AA} is simply the ratio between the spectra at the same transverse momentum. As necessary, for the Z-boson, $R^Z_{\mathrm{AA}} \simeq 1$, while laying between 0.5 and 0.6 for quenched jets, which is compatible with experimental results, evidencing energy losses.

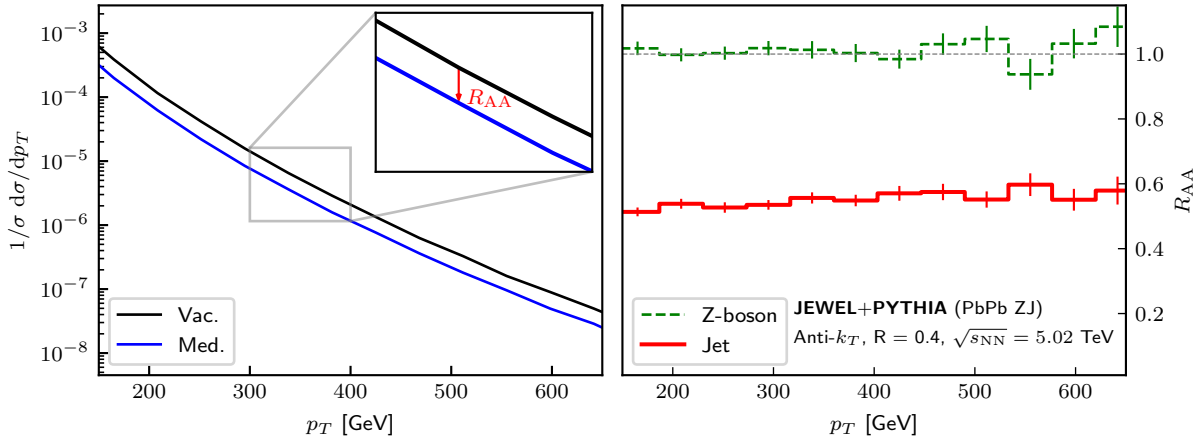

Figure 2.1: (left) Spectrum of vacuum and medium jets, for PbPb collisions with $\sqrt{s_{\mathrm{NN}}} = 5.02$ TeV, in black and blue lines, respectively. The zoomed-in box indicates that the R_{AA} is computed as the ratio between the spectrum of medium and vacuum jets, for a given transverse momentum p_T. **(right)** Nuclear modification factor (R_{AA}) as a function of the transverse momentum, p_T for Z-bosons and jets. Everything was computed using simulated data from JEWEL.

It is worth pointing out that energy loss in a jet does not arise solely from energy loss of individual partons. Due to interactions with the medium, jet particles usually experience deviations from their original trajectories, originating hadrons that will largely deviate from the jet axis, laying outside the reconstruction jet algorithm range. For the same reason, a modification of the particle distribution within the jet is also observed.

2.2 Medium Response

Modifications of jets may manifest not only from their reaction to the QGP, but also from the flip side: the medium's reaction to its crossing through, which we'll refer to as *medium response*. In a hydrodynamical interpretation, a jet traveling through the QGP creates a "moving heated wake" that, by momentum conservation, flows in the same direction as the jet [30], significantly increasing the correlation between the momentum's direction of hadrons formed from the plasma when it freezes out with the jet axis. As a result, some of these hadrons will end up being detected and reconstructed within the final jet.

Even though medium response contributions are expected to be small [31], in terms of momentum increase, these are actually responsible for strong modifications of substructure observables. Evidence for the existence of these effects can be obtained, for instance, by computing these observables using a Monte Carlo event generator, such as JEWEL, through results enabling and disabling the inclusion of medium response contributions in our final state and comparing with actual experimental data. An observable

where medium response shows significant impact is the *jet profile*. Denoting ΔR_{iJ} the geometric distance between a jet particle and the jet axis, this observable is defined by

$$\rho(r) \overset{\text{def}}{=} \frac{1}{p_T^{\text{jet}}} \sum_{i:\ \Delta R_{iJ}=r} p_{T,i}, \tag{2.2}$$

corresponding to a radial momentum distribution inside a jet. In Fig. 2.2, experimental results for the ratio between the jet profile in pp and Pb+Pb collisions are displayed, alongside simulated results in JEWEL, one of which considers the effects of medium response (recoil *on*) and the other discards it (recoil *off*). It is quite visible that the results are only matched when medium response effects in simulations are considered. This result also evidences that the medium response impacts the momentum distribution predominantly on the jet periphery, i.e., for higher distances from the axis.

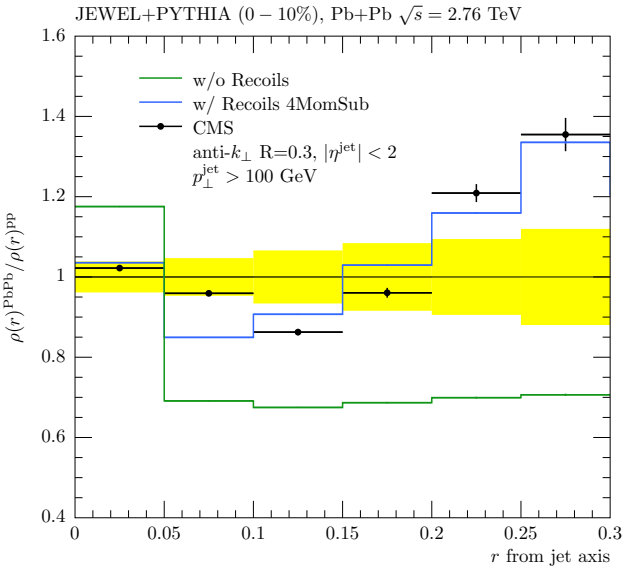

Figure 2.2: Jet profile in Pb+Pb collisions at $\sqrt{s_{\text{NN}}} = 2.76$ TeV, using simulated data from JEWEL+PYTHIA, with and without response effects (blue and green lines, respectively), and data from CMS (dots). The shaded region around the unit represents the uncertainties of simulated data. Taken from [31].

Medium response is a considerable source of uncertainty. If we wish to obtain reliable and true results in our analysis, it is desirable to either be able to disentangle the medium response from the original jet, or to consider observables that are insensitive to this effect. Some desintangling attempts with substructure variables have been tried, but a reliable method is yet to be found. A further motivation to disentangle this response is that, with the medium response particles isolated and in hands, we may be able to study how a perturbation (in this case, the jet passage) triggers the thermalization of the plasma.

2.3 Simulating jets in Heavy-Ion Collisions

The existence of event generators that faithfully simulate the QGP's effects on a jet is crucial in Heavy-Ion studies, given that experimental data is limited and not always available. Many heavy-ion event generators have been developed, most of them based on a PYTHIA parton shower. Examples constitute Hydjet++ [32], JEWEL [33], Q-PYTHIA [34] and JETSCAPE [35]. In the context of this work, we will be considering JEWEL and a hybrid model from [36], to which we'll refer as HYBRID.

JEWEL

JEWEL (Jet Evolution With Energy Losses) is the first and main event generator considered throughout this work. It uses PYTHIA6 as its basis, from where the hard matrix elements, initial state partons and hadronization are simulated. In essence, JEWEL modifies the intermediate showering, where the medium interactions are assumed to take place, simulating jet quenching effects. Quenching, in turn, arises from elastic scattering, described by $2 \to 2$ pQCD matrix elements, and radiation, generated on top of scattering processes.

JEWEL establishes a dictum of describing jet evolution in the QGP using as much perturbation theory in its implementation as possible. In order to achieve this, it is assumed that, in the perspective of the jet, the medium consists of an ensemble of partons. This is naturally mandatory for perturbation theory to take place but also insufficient, since many interactions that can take place between partons are soft, therefore not directly described by pQCD. In order to work around this issue, JEWEL includes the general effect of soft scatterings in the perturbative matrix elements by an analytical continuation of the IR regime, where these interactions can be assumed to take place.

Two additional assumptions are also made regarding radiation effects. Let's suppose that, in an emission step, two or more emissions are allowed. Each emission is assigned with a different formation time, and the assumption is that the emission that actually occurs (i.e. the chosen emission to occur) is the one with *shorter* formation time. The other assumption has to do with the LPM effect that occurs in jet quenching. In essence, subsequent scattering sites can be sufficiently close in a way that these interfere destructively with one another, suppressing gluon emissions, i.e., radiative emissions. This effect is derived in eikonal limit, and the assumption is that this derivation is valid in general kinematics, which is how JEWEL operates.

The QGP medium in JEWEL, by default shaped using a Björken model, is simulated according to some parameters, such as the thermalization time τ_i, corresponding to the time it takes after the collision for the plasma to thermalize, and the initial and critical temperatures of the plasma, T_i and T_c, respectively. Changing temperatures, in particular, is a fundamental capability, given that T_c is related to the scale in which hadronization takes place, and the difference on $T_i - T_c$ controls the amount of quenching. These effects will be analysed in future chapters.

HYBRID

We will now describe the second generator to be used in the context of this work, HYBRID, which employs PYTHIA8 to simulate hard matrix elements and parton showering. In this model, it's assumed that the splitting probabilities during parton showering are the same of the in vacuum, adopting a pure PYTHIA showering approach. An energy loss is then applied parton by parton on the whole shower history, using a formula based on the quenching of a light quark jet in the strongly coupled plasma of $\mathcal{N} = 4$ supersymmetric Yang-Mills (SYM) theory, which has been computed holographically and is given by

$$\frac{dE}{dx} = -\frac{4}{\pi} E_i \frac{x^2}{x_s^2} \frac{1}{\sqrt{x_s^2 - x^2}}, \tag{2.3}$$

where E_i stands for the initial energy of the jet and x_s the distance over which a light quark would lose all its energy, determined by

$$x_s = \frac{1}{2\kappa_{\rm sc}} \frac{E_i^{1/3}}{T^{4/3}}, \tag{2.4}$$

where T is the temperature of the plasma. In $\mathcal{N} = 4$ SYM, $\kappa_{\rm sc}$ is a well-defined constant, while in the context of this generator, it is a free parameter.

The splitting partons are embedded in a medium model of the QGP, with its evolution tracked by relativistic hydrodynamics, from where the temperature T entering Eqs. (2.3) and (2.4) is locally determined. The local medium lives until reaching a critical temperature T_c, which in the HYBRID model is not uniform on the phase space (standard values point to $145 < T_c < 170$ MeV).

2.3.1 Simulating medium response effects

The described implementations on the previous section, for both JEWEL and HYBRID, simulate jet quenching effects, but not medium response. In these generators, simulation of medium response is done separately, constituting an essential (and optional) add-on. The inner workings of simulating medium response effects is fundamentally different in JEWEL and HYBRID, and will be described in this section.

In the case of JEWEL, the effects are associated with the recoiling of the medium partons when scattering with jet partons, for which the recoiling information must be stored. The recoiling process is

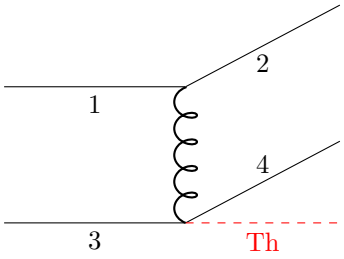

Figure 2.3: Diagrammatic form of a scattering process between jet partons (1 and 2) and medium partons (3 and 4). The thermal parton Th is later stored in the final event.

represented in Figure 2.3, which displays a diagram of a $1 + 3 \rightarrow 2 + 4$ scattering, where 1 and 3 are, respectively, is the jet and medium incident partons.

Choosing to store the recoiling information, the medium recoiled parton (4) is assumed not to further interact and will be queued to hadronization.

The four momentum of the final recoiled parton will be the sum of the thermal momentum, Th, which is stored in the event as partons (gluons), and the transferred momentum from the jet partons. The only component of interest is the latter, so, in events, it is necessary to subtract the thermal component from the recoiled one. This is not directly possible at hadron level, given that recoiled partons hadronize with the whole jet, hence the final jet is not a simple superposition of jet and medium particles and one cannot associate a particle coming from the jet or coming from response. A subtraction technique is therefore required; in this work, we will be using the component subtraction from [31], outlined and technically explored in the Appendix A.

In HYBRID, medium response is simulated using hydrodynamics, based on the previously mentioned idea that a jet creates a moving heated wake in the plasma. As derived in [37], the spectrum of emitted particles from the wake in this model is

$$\begin{aligned} E\frac{d\Delta N}{d^3p} = &\frac{1}{32\pi}\frac{m_T}{T^5}\cosh(y-y_j)\exp\left(-\frac{m_T}{T}\cosh(y-y_j)\right) \\ &\times\left[p_T\Delta P_T\cos(\phi-\phi_j)+\frac{1}{3}m_T\Delta M_T\cosh(y-y_j)\right]. \end{aligned} \tag{2.5}$$

The wake particles are further generated using a Metropolis algorithm, employing conservation of the lost jet energy using Eq. (2.5), with a probability of 95% of generating protons and 5% of generating pions. In some regions of the phase space, the distribution in (2.5) becomes negative. Particles generated in these regions are called "negative" particles, with negative contributions to the energy and momentum of the generated ensemble. Ref. [37] presents a method to deal with negative particles, which is not implemented in the HYBRID version used in the context of this thesis. The actually used method will be outlined in Section 4.

Contrary to JEWEL, the jet partons in HYBRID hadronize without taking into account the medium response (which are pre-generated protons and pions), allowing to distinguish both contributions in the final state.

Given the differences between these models, it should be interesting to compare the medium response signatures from each generator in observables. In Chapter 6, we will be exploring this in energy correlators, which will be introduced and developed in the next chapter.

Chapter 3

Energy Correlators

Until very recently, most observables used in the context of jet studies belonged to the class of *jet substructure observables*, such as the jet profile presented in Chapter 2. While many important results can be obtained by studying such observables, these also possess some limitations and disadvantages. For instance, many substructure observables are introduced in a *ad-hoc* way, sometimes lacking of a real physical interpretation, and may throw away a lot of information. In this chapter, we introduce a novel class of observables, with a more developed origin: the energy correlators.

We begin by presenting a comprehensive study on Energy Flow Correlators, which constitute fundamental field theory objects motivated by conformal field theory (CFT) ideas. The Operator Product Expansion (OPE), an important technique regarding quantum field correlation functions, is, for completeness, also mentioned, in order to familiarize with the language and theoretical techniques used in the context of these functions. Finally, the main observables to be analyzed in this work are defined in terms of this correlator and adapted to the context of jets.

3.1 Theoretical foundations and overview

3.1.1 Localized perturbations and Cross-section

The underlying formalism will be developed by considering a simple scattering process $ij \to f$, where i and j are two incident particles and f the final state of the process.

We begin by introducing a local operator $\mathcal{O}(x)$, which creates a local perturbation that results on the transition of an initial state to a final state. More concretely, and in order to suppress the coordinate dependence, $\mathcal{O}$ can be implicitly defined by expressing the transition matrix element $\mathcal{M}_{ij\to f}$ in terms of this operator [38] evaluated at a chosen reference point (for which we choose the origin), i.e.

$$\mathcal{M}_{ij\to f} \overset{\text{idef}}{=} \langle f|\, \mathcal{O}(0)\, |0\rangle\,. \tag{3.1}$$

The momentum of this operator is defined as the 4-vector k such that $\mathcal{O}(x) = e^{ik\cdot x}\mathcal{O}(0)$. In the case of QED/QCD, the source operator can correspond to, for instance, the electromagnetic current $\bar{\psi}\gamma^\mu\psi$.

The cross-section can be naturally expressed in terms of this operator. Denoting $1/P$ as the factor related to the phase-space of the initial particles, we recall the formula for the cross-section in terms of the matrix element $\mathcal{M}$:

$$\sigma_{\text{tot}}(q) = \frac{1}{P}\sum_f (2\pi)^4 \delta^{(4)}(q - k_f)|\mathcal{M}_{ij\to f}|^2. \tag{3.2}$$

Assuming that the final states of our process obey the closure relation, $\sum_f |f\rangle \langle f| = 1$, the cross-section can be expressed using the localized perturbation operators through

$$\begin{aligned}
\sigma_{\text{tot}}(q) &= \frac{1}{P}\sum_f \int_x e^{i(q-k_f)\cdot x} |\langle f| \mathcal{O}(0) |0\rangle|^2 \\
&= \frac{1}{P}\int_x e^{i(q-k_f)\cdot x} \langle 0| \mathcal{O}^\dagger(0) \left(\sum_f |f\rangle \langle f|\right) \mathcal{O}(0) |0\rangle \\
&= \frac{1}{P}\int_x e^{iq\cdot x} \langle 0| (e^{ik_f\cdot x}\mathcal{O}(0))^\dagger \mathcal{O}(0) |0\rangle \\
&= \frac{1}{P}\int_x e^{iq\cdot x} \langle 0| \mathcal{O}^\dagger(x)\mathcal{O}(0) |0\rangle .
\end{aligned} \tag{3.3}$$

Here, we used the fact that the localized perturbations must possess the 4-momentum of the final state, k_f, by conservation of momentum. This is an important way to write the total cross-section, given that it allows to express certain quantities as Wightmann correlation functions.

3.1.2 Weighted Cross-Sections

Many observables can be expressed using an extension of the concept of cross-section, the *weighted cross-section* [39]. To motivate this definition, we begin noting that, for a region of the phase-space R,

$$\frac{1}{\sigma_{\text{tot}}}\int_R \mathrm{d}\sigma \leq 1, \tag{3.4}$$

with equality for R corresponding to the full phase-space. One can adopt a probabilistic interperation of the quantity in Eq. (3.4), or, more concretely, that an integration over a restricted region of the phase space, divided by the total, returns a fraction of final-state compositions obeying certain conditions.

Distributions, and in particular many experimental observables, can, therefore, be computed by integrating over restricted domains of the phase space, which can be achieved by inserting a Dirac-delta, δ, or a theta function, Θ, inside the integral over all the phase-space, filtering the final states according to what we wish to obtain. For instance, a mass distribution of final state particles writes

$$\frac{1}{\sigma_{\text{tot}}}\int \delta(m - \hat{M})\mathrm{d}\sigma = \frac{1}{\sigma_{\text{tot}}}\frac{\mathrm{d}\sigma}{\mathrm{d}m} \equiv \frac{1}{N}\frac{\mathrm{d}N}{\mathrm{d}M}, \tag{3.5}$$

where the operator $\delta(m - \hat{M})$ selects the final-state particles with mass m. A natural generalization of this is obtained by inserting an arbitrary operator instead, from where one can define the weighted cross-section as

$$\frac{\mathrm{d}\sigma_w}{\mathrm{d}a} \overset{\text{def}}{=} \int \hat{w}(a)\ \mathrm{d}\sigma, \tag{3.6}$$

where a represents (a set of) external variables that the operator $\hat{w}$ may depend on. Using our previous formalism, this observable can also be expressed as

$$\begin{aligned}\frac{\mathrm{d}\sigma_w}{\mathrm{d}a} &= \frac{1}{P}\sum_f (2\pi)^4\delta^{(4)}(q-k_f)w(f;a)|\mathcal{M}_{ij\to f}|^2 \\ &= \frac{1}{P}\int_x e^{iq\cdot x}\,\langle 0|\,\mathcal{O}^\dagger(x)\hat{w}(a)\mathcal{O}(0)\,|0\rangle\,,\end{aligned} \tag{3.7}$$

where we used $\hat{w}\,|f\rangle = w(f;a)\,|f\rangle$, with $w(f;a)$ being the weight of the final state f. This concept will be readily used to define Energy Flow Correlators.

3.1.3 Energy Flow Operator and Correlator

Assuming a discrete final state of on-shell and massless particles, $|f\rangle = |k_1,...,k_n\rangle$, with $k_i^2 = 0$, and working in the center-of-mass of the system, i.e. $\sum_i k_i = q = (q^0,\vec{0})$, the *Energy Flow Operator* can by implicitly defined by its action on the final state via

$$\mathcal{E}(\vec{\boldsymbol{n}})\,|f\rangle \overset{\text{idef}}{=} \sum_i k_i^0\delta^{(2)}(\Omega_{\vec{\boldsymbol{k}}_i} - \Omega_{\vec{\boldsymbol{n}}})\,|f\rangle = e(f;\vec{\boldsymbol{n}})\,|f\rangle\,. \tag{3.8}$$

The weight factor $e(f;\vec{\boldsymbol{n}})$, for a direction $\vec{\boldsymbol{n}}$, is physically interpreted as a flow of energy per unit of solid angle in that same direction. This alone evidences the conformal nature of this operator, where no metric distances are involved, only angular.

It is also possible to extract the exact form of the operator $\mathcal{E}(\vec{\boldsymbol{n}})$, which can be done either from rigorous CFTs arguments, or motivated by an intuitive argument. For the latter, we need to immediately recall the energy-stress tensor $T_{\mu\nu}(x)$ operator and its interperation.

The time components $T_{0i}(x)$, with $i = 1,2,3$, encode the momentum flux[1], which in the massless limit corresponds to an energy flux, in each i direction. The energy flux in a direction $\vec{\boldsymbol{n}}$ at a given space-time point can be computed by taking the inner product $(T_{01},T_{02},T_{03})\cdot\vec{\boldsymbol{n}} \equiv T_{0i}n^i$. Given the conformal nature of this operator, it is desirable to suppress any distance dependence. For that matter, we evaluate the flux on a space-time point $x^\mu = (t, r\vec{\boldsymbol{n}})$ taking the limit $r\to\infty$. This yields the energy flux on a direction $\vec{\boldsymbol{n}}$ at infinity; the energy flow is obtained by taking the product with the flux area and integrating over time. The area would be[2] $4\pi r^2$, and the factor of 4π is suppressed given that we are taking the flow per unit of solid angle, as in Eq. (3.8). Hence, the energy flow operator writes

$$\mathcal{E}(\vec{\boldsymbol{n}}) = \lim_{r\to\infty}\int_0^\infty r^2 n^i T_{0i}(t, r\vec{\boldsymbol{n}})\mathrm{d}t. \tag{3.9}$$

Energy flow operators are local, and commute when evaluated at different directions, i.e.,

$$[\mathcal{E}(\vec{\boldsymbol{n}}_i),\mathcal{E}(\vec{\boldsymbol{n}}_j)] = 0 \tag{3.10}$$

allowing to compute the operator at different directions independently. Hence, the product of N energy

[1] Flow per unit of area and time.

[2] Note that this area does not break the conformal nature of the operator, given that r is already being taken to infinity.

flow operators admits a simple weight factor

$$\mathcal{E}(\vec{\boldsymbol{n}}_1)...\mathcal{E}(\vec{\boldsymbol{n}}_N)\,|f\rangle = e(f;\vec{\boldsymbol{n}}_1)...e(f;\vec{\boldsymbol{n}}_N)\,|f\rangle \equiv E(f;\vec{\boldsymbol{n}}_1,...,\vec{\boldsymbol{n}}_1)\,|f\rangle\,. \tag{3.11}$$

Using the concept of weighted cross-section, the *N-point Energy Flow Correlator* [40] is defined by

$$\langle\mathcal{E}(\vec{\boldsymbol{n}}_1)...\mathcal{E}(\vec{\boldsymbol{n}}_N)\rangle \overset{\text{def}}{=} \frac{1}{\sigma_{\text{tot}}(q)}\frac{\mathrm{d}\sigma_E(q)}{\mathrm{d}[\vec{\boldsymbol{n}}_1,...,\vec{\boldsymbol{n}}_N]} = \frac{\int_x e^{iq\cdot x}\,\langle 0|\,\mathcal{O}^\dagger(x)\mathcal{E}(\vec{\boldsymbol{n}}_1)...\mathcal{E}(\vec{\boldsymbol{n}}_N)\mathcal{O}(0)\,|0\rangle}{\int_x e^{iq\cdot x}\,\langle 0|\,\mathcal{O}^\dagger(x)\mathcal{O}(0)\,|0\rangle}. \tag{3.12}$$

The definition on Eq. (3.12) evidences the double nature of the Energy Flow Correlator: as a weighted cross-section (divided by the total cross-section), useful for experimental setups, and as a Wightmann correlation function of the operator $\mathcal{E}(\vec{\boldsymbol{n}})$, which, being expressed in terms of stress-energy tensor, is very suitable for theoretical predictions using QFT and CFT techniques. Finally, we can write the Energy Flow Correlator explicitly as

$$\langle\mathcal{E}(\vec{\boldsymbol{n}}_1)...\mathcal{E}(\vec{\boldsymbol{n}}_N)\rangle = \frac{1}{\sigma_{\text{tot}}}\sum_n\sum_{f_n}\sum_{0\le i_1,...,i_n\le n}\int \mathrm{d}\sigma_{ij\to f_n}\prod_{l=1}^{k} k_{i_l}^0\,\delta^{(2)}(\Omega_{\vec{\mathbf{k}}_i}-\Omega_{\vec{\mathbf{n}}_l}), \tag{3.13}$$

where f_n correspond to final states with n particles.

3.1.4 Operator Product Expansion

In QFT, an Operator Product Expansion (OPE) stands for the ability of replacing products of local operators, evaluated at different and close points in space-time, by a combination of composite local operators, inside correlation functions. Formally, denoting $\{\mathcal{O}_k\}$ the set of every operator in a given theory, the OPE between $\mathcal{O}_i(x_i)$ and $\mathcal{O}_j(x_j)$, with $x_i \to x_j$, writes

$$\mathcal{O}_i(x_i)\mathcal{O}_j(x_j) \overset{\text{OPE}}{\sim} \sum_k C_{ijk}(x_i - x_j)\mathcal{O}_k(x_j). \tag{3.14}$$

Under all its restrictions, the OPE is a useful technique to compute correlation functions: one iteration reduces N-point correlation functions to a combination of $(N-1)$-point functions. Recursively, it is possible to express any correlation function (in the close-distance limit) as a combination of one-point functions. This, however, comes with a great cost: the knowledge of the coefficients C_{ijk}, which in general QFTs are extremely challenging to compute. The OPE is also more powerful in CFTs, where the close-distance restriction can be lifted (in a sense, many QFT close-distance limits constitute a conformal limit) and sophisticated techniques can be used to find the coefficients C_{ijk}, e.g. the conformal bootstrap [41].

Regardless of all these limitations in QFTs, OPEs are still particularly useful for the case of energy flow operators[3], as it allows to write a product of these operators in terms of *light-ray operators*, in the collinear limit.

The spin-J light-ray operator $\mathbb{O}^{[J]}(n,\epsilon)$ is defined in terms of spin-J, transverse spin-j and mass

[3] This is much due to the constant fortunate interplay between CFTs and QFTs in the context of energy flow operators

dimension Δ local primary[4] operators $\mathcal{O}^{\mu_1,\ldots,\mu_J,\nu_1,\ldots,\nu_j}(x)$, through

$$\mathbb{O}^{[J]}(n,\epsilon) \equiv \mathbb{O}^{[J]}(\vec{\boldsymbol{n}},\epsilon) \stackrel{\text{def}}{=} \lim_{r\to\infty} r^{\Delta-J}\mathcal{O}^{\mu_1,\ldots,\mu_J,\nu_1,\ldots,\nu_j}(t,r\vec{\boldsymbol{n}})\ \bar{n}_{\mu_1}\ldots\bar{n}_{\mu_J}\epsilon_{\nu_1}\ldots\epsilon_{\nu_j}, \tag{3.15}$$

where $n=(1,\vec{\boldsymbol{n}})$, $\bar{n}=(1,-\vec{\boldsymbol{n}})$ and ϵ a polarization vector such that $\epsilon^2=\epsilon\cdot n=\epsilon\cdot\bar{n}=0$. In terms of these operators, the energy flow operators' OPE is dominated by spin-3 light-ray operators, taking the form, in the collinear limit and denoting $\theta_{12}\ll 1$ as the angle between $\vec{\boldsymbol{n}}_1$ and $\vec{\boldsymbol{n}}_2$,

$$\mathcal{E}(\vec{\boldsymbol{n}}_1)\mathcal{E}(\vec{\boldsymbol{n}}_2) \overset{\text{OPE}}{\sim} \frac{\alpha_s}{\pi}\sum_i\ C_i\ \theta_{12}^{\lambda_i}\ \mathbb{O}_i^{[3]}(\vec{\boldsymbol{n}}_2)+\mathcal{O}(\theta_{12}^2)^0 \tag{3.16}$$

where the exponent $\lambda_i=(\tau_i-4)$, with $\tau_i=\Delta_i-J$ denoting the *twist* of the light-ray operator. At LO leading twist, corresponding to $\tau_i=2$, the correlator is dominated by an angular dependence of $\sim 1/\theta_{12}^2$, and higher twists produce sub-leading order terms.

OPE is currently the main theoretical technique used to make predictions on the behavior of correlators in the perturbative regimes throughout the literature. Reference [42] presents a very detailed computation of the OPE in vacuum, including the OPEs of $\mathcal{E}(\vec{\boldsymbol{n}}_1)\mathbb{O}(\vec{\boldsymbol{n}}_2)$ and $\mathbb{O}(\vec{\boldsymbol{n}}_1)\mathbb{O}(\vec{\boldsymbol{n}}_2)$ and resummation up to NLL. In [43, 44], the first predictions using results from OPEs in heavy-ion collisions are presented, also marking the beginning of using energy correlators to probe the QGP.

Throughout this work we will use energy flow correlators to define observables that can be computationally determined inside jets. In next section, these observables will be presented. Even though the OPE is not going to be directly used in this analysis, such observables can also be predicted using results form it [45, 46].

3.2 Energy Correlators inside Jets

The energy flow correlator as presented in Eq. (3.13) is too complex to be fully determined. Not only it depends on too many variables (each vector $\vec{\boldsymbol{n}}$ requires 2 angles to be fully described), but also encodes too much information that may complicate a physical interpretation. Hence, it is imperative to define simpler observables with more immediate interpretations that can be extracted from this correlator and measured experimentally.

The most widely used classes of observables at present are the projected correlators [47], wherein the $N-$point correlators are projected into a scale x_L, by integrating in all $\vec{\boldsymbol{n}}_i$ and keeping x_L fixed, i.e.,

$$\frac{1}{\sigma}\frac{\mathrm{d}\sigma_{\text{ENC}}}{\mathrm{d}x_L} \equiv \int\left(\prod_{i=1}^{N} d\Omega_{\vec{\boldsymbol{n}}_i}\right)\frac{\langle\mathcal{E}(\vec{\boldsymbol{n}}_1)\ldots\mathcal{E}(\vec{\boldsymbol{n}}_N)\rangle}{Q^N}\delta(x_L-\hat{x}_L), \tag{3.17}$$

where Q is an arbitrary energy scale.

In the context of jets - our objects of study - this observable needs to be adapted, in order to faithfully correspond to what we have built in the previous sections. To evaluate these correlations inside jets, each jet in a final event can be roughly considered as an independent final state. However, this can only be

[4] Not expressed as derivatives of other operators

achieved when using $k^0 \to p_T$ and $q^0 \to p_T^{\rm jet}$, which is the jet's equivalence to the CoM requirement used in Eq. (3.8). The projection scale of interest is the longest side R_L, corresponding to the highest pair-wise distance ΔR_{ij} for each tuple of N particles. For instance, the 2-point projection inside jets of transverse momentum $p_T^{\rm jet}$, considering $Q = p_T^{\rm jet}$, is given by

$$\frac{1}{\sigma}\frac{\mathrm{d}\sigma_{\rm EEC}}{\mathrm{d}R_L} = \sum_{i,j}\int \frac{d\sigma(\Delta R_{ij})}{\sigma}\frac{p_{T,i}p_{T,j}}{(p_T^{\rm jet})^2}\delta(R_L - \Delta R_{ij}). \tag{3.18}$$

From a set of events, such observable can be computed by filling a histogram on the R_{ij}, where each entry corresponds to a pair (i,j) of final state particles and is weighted with $p_{T,i}p_{T,j}/(p_{T,\rm jet})^2$. The normalization of the histogram is arbitrary; in the context of this work, we will be using the *per jet* prescription, i.e., normalized by the number of jets[5]. These distributions will be referred to as the *Energy-Energy Correlations*, EEC, also denoted as $\frac{1}{N_{\rm jet}}\frac{\mathrm{d}\sigma}{\mathrm{d}R_L}$, and can be computed through

$$\mathrm{EEC}\left((R_L)^{\pm\delta}\right) = \frac{1}{N_{\rm jet}}\sum_{\rm evts,jets}\sum_{i,j\in{\rm jet}}\frac{p_{T,i}p_{T,j}}{(p_T^{\rm jet})^2}\,\frac{\Theta(R_{ij}\in[R_L-\delta, R_L+\delta])}{2\delta}, \tag{3.19}$$

where $(R_L)^{\pm\delta}$ denotes the histogram bin $[R_L-\delta, R_L+\delta]$.

Qualitatively, the EEC is expected to manifest the different phases that jet's constituents went through, from hadronic to partonic, given that, for instance, lower scale correlations are obtained through pairs of particles that are close to each other, which is possible only after the phase space is sufficiently filled - usually, only after the hadronization process. Higher scales would also correspond to signatures of the partonic phase.

It is also interesting to consider higher-point correlations, denoted by ENC, where this time, the histogram is filled on the largest distance R_L of a N-tuple of particles weighted by $p_{T,i_1}...p_{T,i_N}/(p_T^{\rm jet})^N$. In Figure 3.1, a sketch indicating how the histograms for the cases EEC and E3C are filled is displayed.

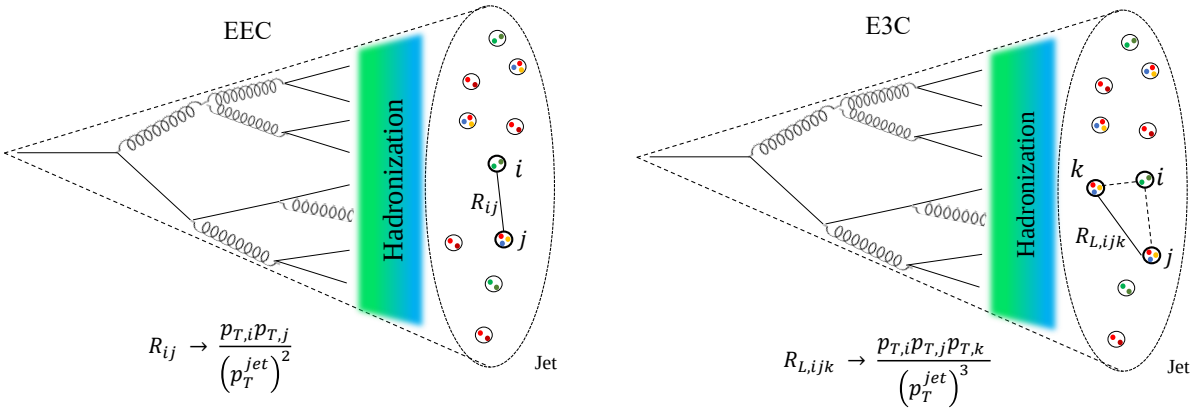

Figure 3.1: Computation of the EEC and E3C inside jets schematized. In the case of the EEC, it is indicated that the histogram bins correspond to distances between pairs (i,j) R_{ij}, filled with weight $p_{T,i}p_{T,j}/(p_T^{\rm jet})^2$, while in the E3C, the histogram bins correspond to the longest distance in a triple (i,j,k), $R_{L,ijk}$, filled with weight $p_{T,i}p_{T,j}p_{T,k}/(p_T^{\rm jet})^3$. The phases of QCD matter, also represented in the figure, are manifested in these functions.

[5] This way, we are in fact computing correlations *inside* jets.

One can also motivate the definition of other observables from the EEC. As an example, we can define a logarithmic Energy-Energy Correlation, $\mathrm{EEC}_{\ln}$, by

$$\mathrm{EEC}_{\ln}(R_L) \stackrel{\mathrm{def}}{=} R_L \mathrm{EEC}(R_L) \equiv \frac{1}{N_{\mathrm{jet}}} \frac{\mathrm{d}\sigma_{\mathrm{EEC}}}{\mathrm{d}\ln R_L}, \tag{3.20}$$

which enhances the correlation function at higher scales, i.e. at the partonic phase. Another useful extension of the EEC is the weighted Energy-Energy Correlation, $\mathrm{EE}^n\mathrm{C}$, where a power n is placed on the momentum dependence of the correlation,

$$\mathrm{EE}^n\mathrm{C}\left((R_L)^{\pm\delta}\right) = \frac{1}{N_{\mathrm{jet}}} \sum_{\mathrm{evts,jets}} \sum_{i,j\in\mathrm{jet}} \frac{p_{T,i}^n p_{T,j}^n}{(p_T^{\mathrm{jet}})^{2n}} \frac{\Theta(R_{ij} \in [R_L - \delta, R_L + \delta])}{2\delta}, \tag{3.21}$$

which can enhance or suppress higher or lower momentum particles depending on the choice of n. For instance, with $n > 1$, we could expect to suppress the medium response contributions, given that these are dominated by hadrons with low momentum.

The last class of observables with immediate interest are the ratios between N-point and M-point correlation functions, given and denoted by

$$\mathrm{R}_{\mathrm{EC}}^{[N,M]} \stackrel{\mathrm{def}}{=} \frac{\mathrm{ENC}(R_L)}{\mathrm{EMC}(R_L)} \equiv \frac{\mathrm{d}\sigma_{\mathrm{ENC}}}{\mathrm{d}\sigma_{\mathrm{EMC}}}. \tag{3.22}$$

These ratios are expected to be more robust experimentally, due to the approximate cancelation of undesired effects, such as hadronization corrections.

Finally, it is worth pointing out that all these observables are IRC safe, allowing us to properly use them in phenomenological studies.

Chapter 4

Computational setup and techniques

We will now describe the computational setup and techniques used to obtain the results presented in the following chapters, namely treatment of events, jet reconstruction details alongside particularities of each generator. We begin by describing the common procedures to every event type, and later consider Z+jet events in its own section, where extra steps must be considered in order to identify the Z-boson from the event.

4.1 Event processing and Jet Reconstruction

In usual simulated event files, the different particles are stored in the form of the momentum components, energy, PDG id, and other useful information that the different generators find relevant to store, such as customized labels.

Event files from JEWEL and HYBRID are fundamentally different. JEWEL admits only one event file for each generation configuration (e.g. vacuum, medium without response and medium with response), while in HYBRID, the output file contains a full event: particles from a pp collision, labeled as 5, the corresponding medium-modified particles, labeled as 0, and particles arising from medium response, labeled as 1 ("positive" particles) and -1 ("negative" particles).

In both generators, initial-state particles are also stored in event files. This is easy to maneuver, given that these have specific labels that distinguish them from final-state particles. The final-state particles of interest are then stored in lists, each in the form of `Pseudojet`, which is the 4-momentum container for `FastJet`. At this level, two cuts are applied: to only store particles with $p_T > 0.5$ GeV and with an absolute rapidity of $|y| < 3.3$. Particles from the list are further submitted to jet reconstruction.

Events with medium response require an intermediate step. In JEWEL, the thermal particles introduced in Chapter 2, which have a particular label, are stored in a different list from the rest of the particles of interest. The subtraction method as described in Appendix A is then applied, and the resulting list of particles constitute the one to be submitted for reconstruction. In the case of HYBRID, we set in the recombination algorithm to consider negative particles as negative contributions to the recombined momentum.

`FastJet` also allows to attribute a customized label to each particle (`Pseudojet`) in the list. This is particularly useful in HYBRID, in order to save the information that is contained in the event files on the class of a particles (e.g. particles coming from medium response). This information is not lost after jet reconstruction, which constitutes the next step.

Treatment of jets was fully performed using the `FastJet` library throughout the entirety of this work. In every case of analysis to be considered, jets were reconstructed using the Anti-k_T algorithm, with a reconstruction radius of $R = 0.4$. A cut on the jet's rapidity was included: $|y_{\text{jet}}| < 2.8$. Reconstructed jets are further stored in a list of jets, in the form of `Pseudojet`, ordered by transverse momentum. `FastJet` is endowed a plethora of methods that allow to access information about each jet, such as the constituents, which themselves belong to the `Pseudojet` class and benefit from the same methods, transverse momentum, mass, rapidity, etc., which can be used to compute, for instance, the energy correlation functions using Eq. (3.19).

4.2 Z+jet events

Events with bosonic final-state particles, such as Z+jet events, require a separate analysis in order to identify the final boson.

In these generators, Z-bosons are set to decay into $\mu^+\mu^-$ pairs, and these particles are stored in the event file. Using the PDG id information contained in the events, muons and anti-muons are stored in separate lists, not interfering with hadrons that will participate on the jet clustering. An invariant mass interval allowed for the final Z-boson is defined, for which we choose $[70, 115]$ GeV. The procedure is then to identify the most energetic muon/anti-muon pair out of the two lists (list of muons and list of anti-muons), whose mass is contained in the invariant mass window and simultaneously passes the transverse momentum cuts. Z+jet events where no valid Z-boson is identified are excluded from analysis.

Chapter 5

Vacuum vs. Medium results

The results of the EEC for jets in pp collisions (vacuum jets) and jets in PbPb collisions (medium jets) are presented in this chapter. For this analysis, we will be neglecting effects of medium response, which will be separately studied in the next chapter.

We begin by presenting the adopted methodology, proceeded by an analysis of the vacuum jet results. These results have shown the different QCD phases imprinted on the correlation function and ratios. Then, a comparison with medium results is made, and the differences on both signatures are studied in detail. The major difference encountered between vacuum and medium jets was a shift on the EEC's distribution peak, which could be related to a delay of the transition phase (a hadronization delay), and is analyzed in detail. The chapter closes with a summary of the main results.

Throughout this chapter, JEWEL will be used as the main event generator, given the availability of a wide variety of events with different generation conditions; HYBRID results will be presented whenever found relevant.

5.1 Methodology: overcoming migration of jets

Migration is a phenomenon where jets with certain original characteristics (to which the transverse momentum p_T is a proxy) will shift (migrate) towards a different p_T when given modifications due to external interactions. The most natural example is the study of jets that travel through the QGP; the p_T of such jet would be remarkably different if the jet hadn't gone through quenching. Another example of great importance is the effect of medium response, since it is expected to increase a jet p_T by a few GeV, which will be discussed in the next chapter. This migration effect must be seriously considered if one intends to make faithful comparisons between sets of jets, given that it has great influence in the final results and constitutes one the biggest source of uncertainties. In this section, methods to deal with migration of jets will be established. Naturally, for statistical reasons, one cannot analyze jets with fixed p_T; instead, short p_T-windows are considered.

The first method uses the Q_{AA} observable from [48], particularly useful in the context of dijet events. Considering jets from pp collisions (vacuum) and the corresponding jets with quenching modifications

(medium), from AA collisions, we define the $Q_{\rm AA}$ as the p_T ratio of vacuum and medium jets laying in the same quantile of equal probability, i.e.,

$$Q_{\rm AA} \overset{\rm def}{=} \left.\frac{p_T^{\rm med.}}{p_T^{\rm vac.}}\right|_{\Sigma^{\rm eff}}. \tag{5.1}$$

In a simplified picture, this observable compares statistical equivalent vacuum and medium jets (with and without quenching), with the same (upper) cumulative effective cross-section, in turn defined by

$$\Sigma^{\rm eff}(p_T) \overset{\rm def}{=} \int_{p_T}^{\infty} {\rm d}p'_T \frac{{\rm d}\sigma^{\rm eff}}{{\rm d}p'_T}. \tag{5.2}$$

Given a medium jet with momentum $p_T^{\rm med}$, we define the *quantile momentum* $p_T^{\rm quant}$ as the momentum of a vacuum jet with the same cumulative effective cross-section,

$$\Sigma^{\rm eff}_{\rm vac}(p_T^{\rm quant}) \equiv \Sigma^{\rm eff}_{\rm med}(p_T^{\rm med.}), \tag{5.3}$$

which, in this framework, can be interpreted as the momentum of the corresponent vacuum jet (without the medium modifications). Using the $Q_{\rm AA}$, we can naturally establish

$$p_T^{\rm med.} = p_T^{\rm quant} Q_{\rm AA}(p_T^{\rm quant}). \tag{5.4}$$

In the context of this chapter, this method will be mainly adopted for dijet events in JEWEL, comparing vacuum and medium jets with default settings $(T_i, T_c) = (0.55, 0.17)$ GeV. Figure 5.1 displays the cumulative cross-section $\Sigma^{\rm eff}$ and the corresponding $Q_{\rm AA}$. Using these results, a vacuum jet p_T-window

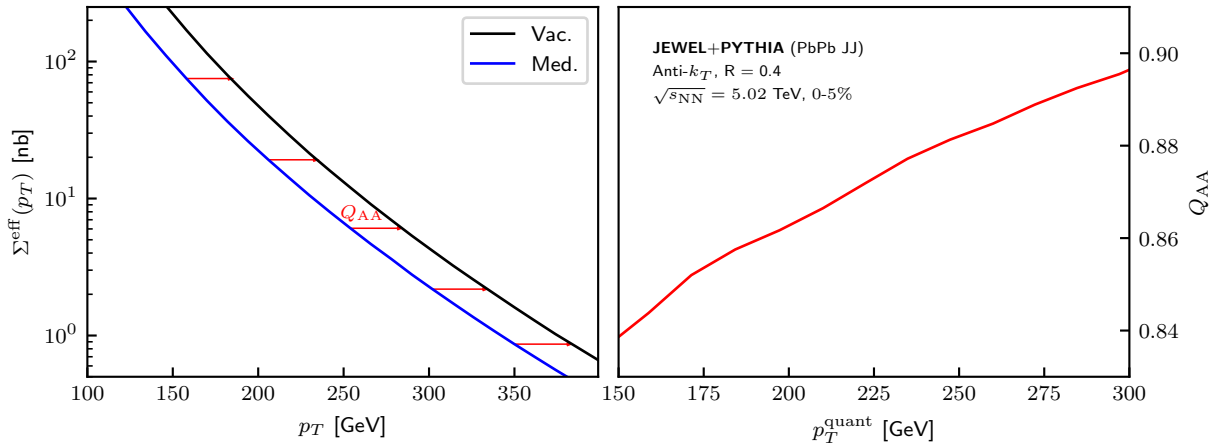

Figure 5.1: (left) Cumulative cross-section as a function of p_T, for vacuum (blue line) and medium (black line) jets. The arrows indicate that the $Q_{\rm AA}$ is computed by taking the ratio between the p_T of medium and vacuum with the same $\Sigma_{\rm eff}$. **(right)** The corresponding $Q_{\rm AA}$, as a function of the quantile momentum, $p_T^{\rm quant}$.

$[200, 240]$ GeV would approximately correspond to a medium jet window

$$[200 \times Q_{\rm AA}(200\ {\rm GeV}),\ 240 \times Q_{\rm AA}(240\ {\rm GeV})]\ {\rm GeV} \simeq [170, 208]\ {\rm GeV}.$$

A crucial observation is that this is an average method, since not all medium jets inside a window computed using the Q_{AA} are counterparts of jets in the initial ensemble of vacuum jets, and some actual medium counterparts will fall out of this window. These effects are, however, expected to be small, but one cannot take this method as the most accurate.

Given this issue, a second method, exclusive to γ+jet or Z+jet events, is used. The idea is that jets associated with a fixed p_T of the tagged boson (γ or Z) had a similar hard origin, given that the p_T of the boson, which does not interact with the medium, is related to the p_T of the hard process. One of the disadvantages of this method is that jets associated with a fixed boson-p_T may belong to a wide p_T-window, both in the cases of vacuum and medium jets. This can be mitigated by considering very energetic jets, where a fixed boson-p_T provides a sufficiently narrow p_T window of jets. Another disadvantage is that either γ+jet or Z+jet events are far less probable than dijet events, motivating the development and usage of methods in dijet events. In the context of MC event generators, this is not an issue; however, motivated by experimental limitations, methods for both outcomes will be implemented and analyzed.

5.2 Vacuum results

In this section, results for the EEC in pp collisions (vacuum) will be analyzed. Figure 5.2 displays the EEC in dijet events, for $p_T \in [200, 240]$ GeV.

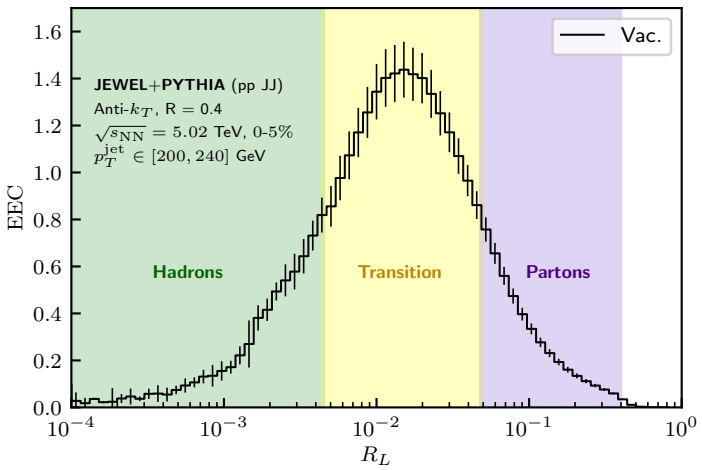

Figure 5.2: EEC in pp collisions, inside jets with $p_T^{\mathrm{vac}} \in [200, 240]$ GeV, using simulated data from JEWEL. The shaded regions represent different QCD regimes according to the R_L scale. Error bars are statistical only. The partonic region is identified up to $R_L = R_{\mathrm{jet}} = 0.4$.

As predicted in Chapter 3, the EEC manifests different signatures for the QCD matter phases: partonic regime in higher scales ($R_L \gtrsim 10^{-1}$), a transition (hadronization) in intermediate scales and the hadronic phase in lower scales ($R_L \lesssim 10^{-3}$). This interpretation is enhanced when analyzing the EEC at parton level, where the final state particles didn't go through the hadronization process, displayed in Figure 5.3.

At this level, a strong suppression on the lower and intermediate scales is observed, and correlations approach the hadron-level counterpart at higher scales, evidencing that most contributions on the higher

scales are characteristic of the partonic phase.

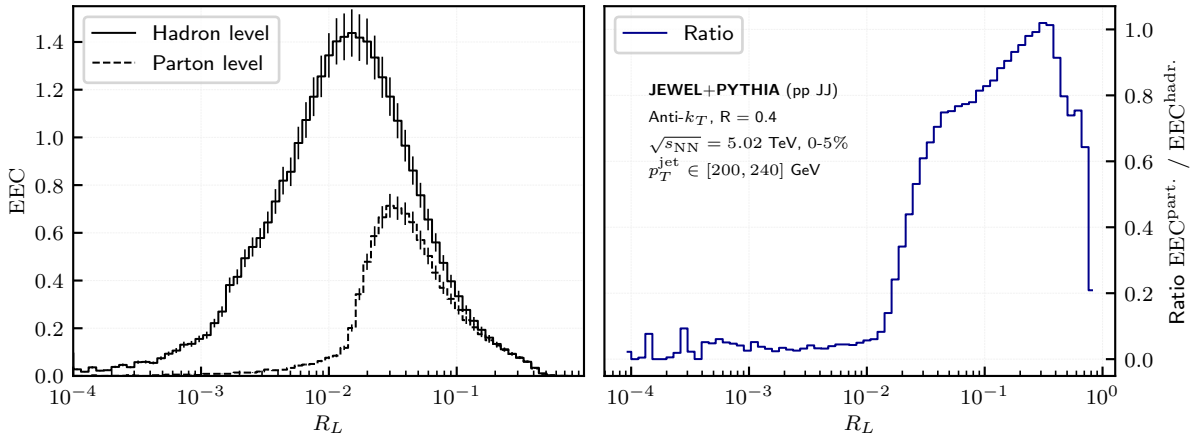

Figure 5.3: (left) EEC in pp collisions, inside jets with $p_T^{\rm vac} \in [200, 240]$ GeV, using simulated data from JEWEL, at hadron (solid line) and parton (dashed line) levels. **(right)** Ratio between the EEC at parton and hadron level.

When considering vacuum jets with different transverse momenta, a horizontal shift of the distributions' peaks is observed, as in Figure 5.4 **(left)**. This shift arises from the observation that the momentum scale where the transition occurs is (in the vacuum) $p_T^{\rm jet} R_L \sim \Lambda_{\rm QCD}$ [49]; therefore, the scale R_L where the transition occurs is inversely proportional to the jet p_T. A way to illustrate this effect is achieved by rescaling $R_L \to p_T^{\rm jet} R_L$, as displayed in Figure 5.4 **(right)**, where we observe the peaks aligning. In terms of jet substructure, this result evidences that jets with higher transverse momentum possess a narrower spatial momentum distribution, given that hadrons are closer to one another, which also leads to an increase of the absolute EEC value.

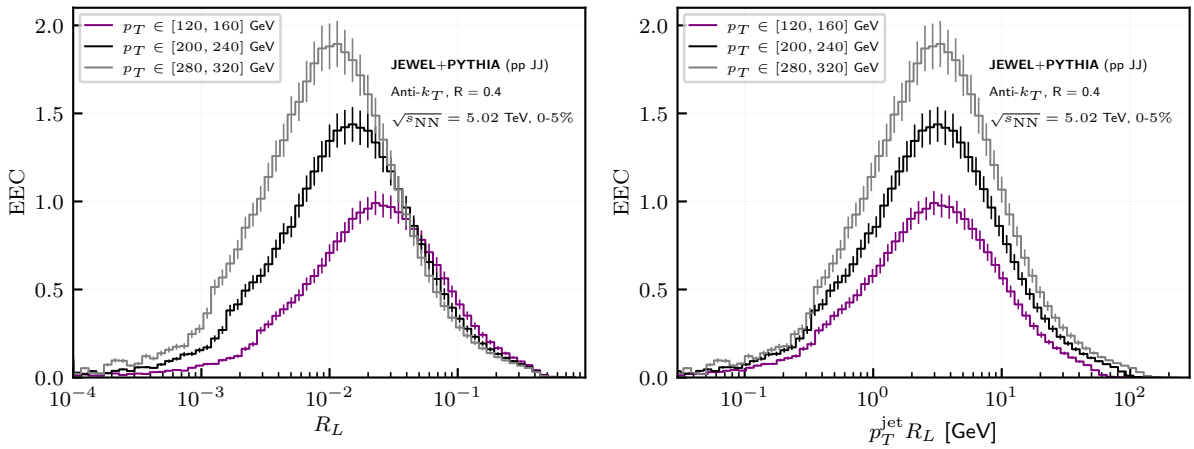

Figure 5.4: (left) EEC in pp collisions, inside jets with $p_T^{\rm jet} \in [120, 160]$ GeV (purple line), $p_T^{\rm jet} \in [200, 240]$ GeV (black line) and $p_T^{\rm jet} \in [280, 320]$ GeV (grey line), using simulated data from JEWEL. **(right)** Corresponding EEC with the R_L rescaled to $p_T^{\rm jet} R_L$, where the alignment of the peaks is observed.

It should also be worth to explore higher point correlation functions, such as E3C and E4C. Usually, these higher-point correlation functions alone do not show any new interesting behavior; however, the ratios $\rm R_{EC}^{[N,M]}$ put in evidence the interesting features of considering higher points. Figure 5.5 shows the

ratios $R_{EC}^{[3,2]}$ and $R_{EC}^{[4,2]}$, for the previous jets.

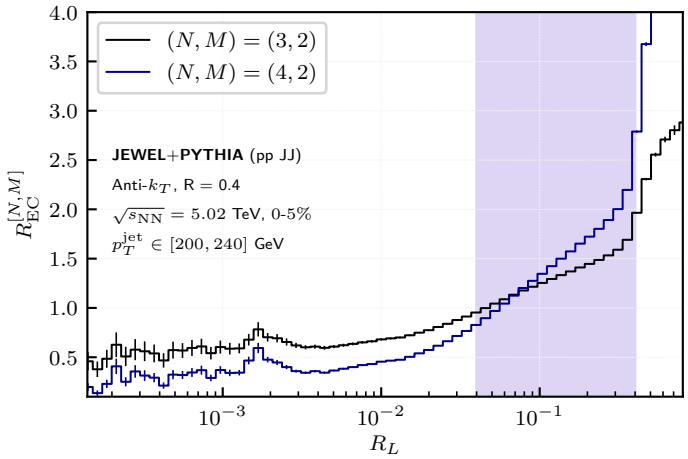

Figure 5.5: Ratios $R_{EC}^{[N,M]}$ inside jets vacuum with $p_T^{jet} \in [120, 160]$ GeV (purple line), $p_T^{jet} \in [200, 240]$ GeV (black line) and $p_T^{jet} \in [280, 320]$ GeV (grey line), using simulated data from JEWEL.

Similarly to the EEC, the ratios are shown to display characteristic signatures for the different phases, specially for the partonic regime, where a linear behavior with $\log(R_L)$ is evidenced.

We can also verify the dependence of the ratios' shape with the jet p_T, as was done with the EEC. This will be shown for $R_{EC}^{[3,2]}$; the behavior for higher points is similar. The results are displayed in Figure 5.6.

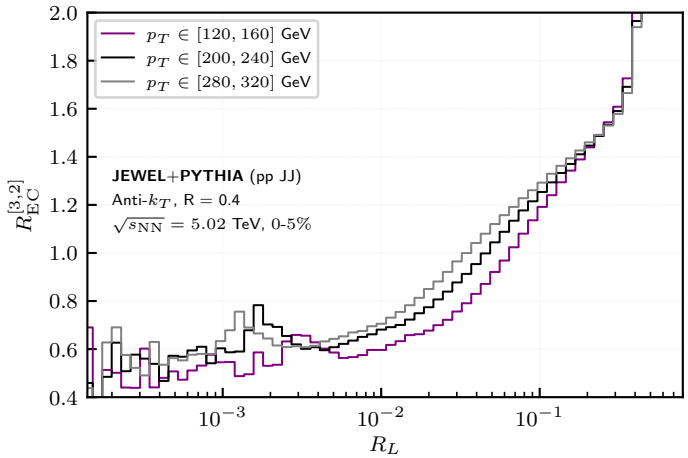

Figure 5.6: Ratio $R_{EC}^{[3,2]}$ inside vacuum jets, for different with $p_T^{jet} \in [120, 160]$ GeV (purple line), $p_T^{jet} \in [200, 240]$ GeV (black line) and $p_T^{jet} \in [280, 320]$ GeV (grey line), using simulated data from JEWEL.

From these results, it is shown that with the increase of the jet p_T, the "slope" of the linear regime decreases. This behavior is compatible with the observed displacement of the peaks. Since the EEC's peak for higher jet p_T shifts towards a lower R_L scale, it would be expected that the partonic phase is manifested for longer ranges of R_L, hence a decrease of the slope observed in the ratios (also noting that all the ratios approach the same value near the jet radius $R = 0.4$).

5.3 Medium vs. Vacuum

We will now study the effects of the QGP medium on the EEC. Beginning with dijet events, in Figure 5.7 we display the results for the previous case of jets in vacuum, with $p_T \in [200, 240]$ GeV, and its (approximate) medium modified counterpart, using JEWEL's default settings ($T_i = 0.55$ GeV, $T_c = 0.17$ GeV), corresponding to $p_T \in [170, 208]$ GeV by the Q_{AA} method as outlined in section 5.1.

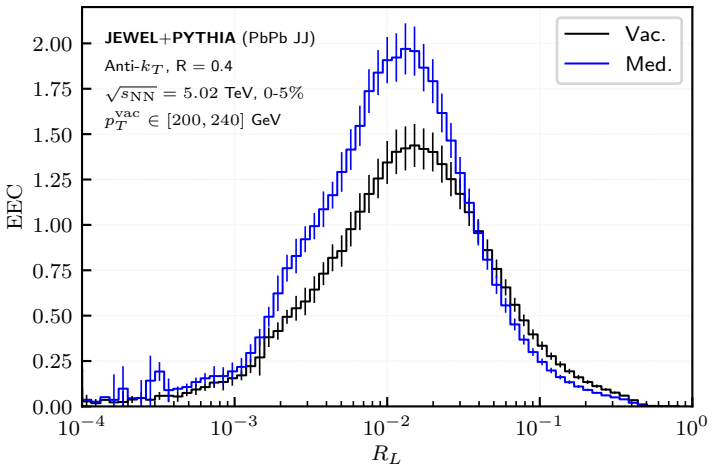

Figure 5.7: EEC inside medium jets with $p_T^{\mathrm{med}} \in [170, 208]$ GeV (blue line), correspondent to vacuum jets with $p_T^{\mathrm{vac}} \in [200, 240]$ by the Q_{AA} method (also displayed in black line), using simulated data from JEWEL. Error bars are statistical only.

Two effects are observed in the EEC: first, a slight shift on the distribution's peak, which is clearer when the normalization of the EEC is rescaled in order to coincide the value of the maxima, as in Figure 5.8; secondly, an enhancement of the EEC at lower scales, and consequential suppression at higher scales.

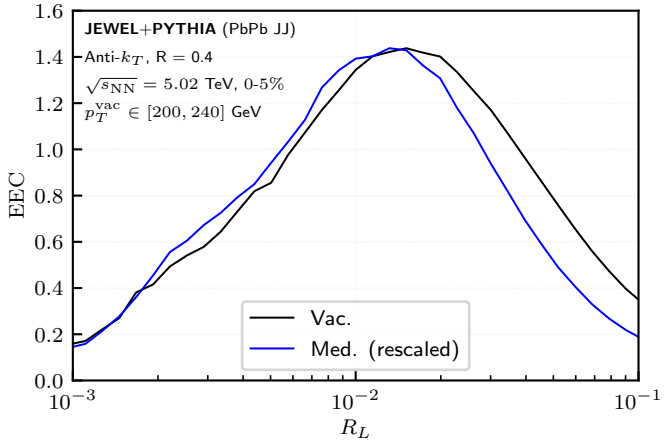

Figure 5.8: EEC inside medium jets with $p_T^{\mathrm{med}} \in [170, 208]$ GeV (blue line), correspondent to vacuum jets with $p_T^{\mathrm{vac}} \in [200, 240]$ by the Q_{AA} method (also displayed in black line), rescaled in order for the maximum of EEC in vacuum to coincide with the maximum the EEC in medium. Error bars are omitted for visualization purposes.

In order to further investigate these effects, in Figure 5.9, the results at parton level are presented.

These suggest that hadrons play a more meaningful role on the higher scales when compared to its vacuum counterpart, even though it is still dominated by partons. The overall contribution of partonic signatures is also reduced.

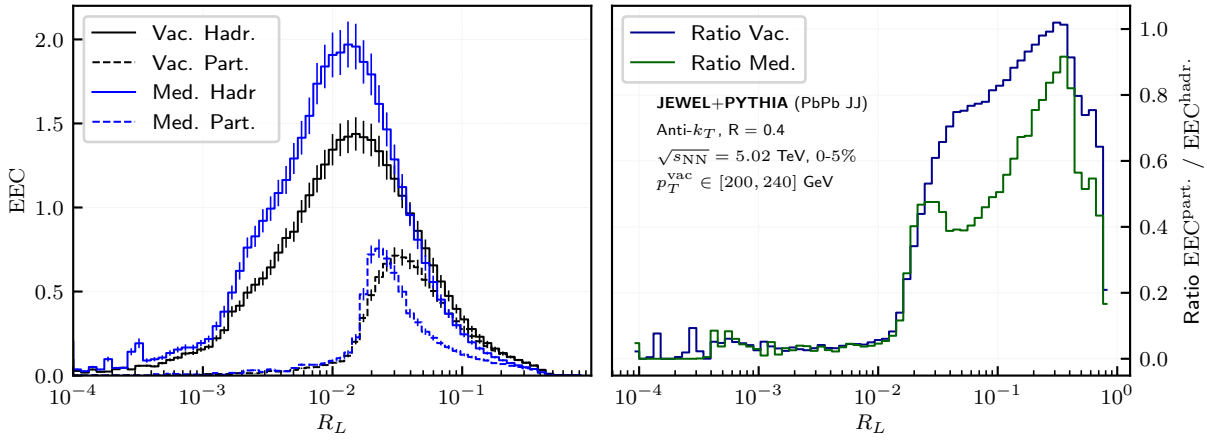

Figure 5.9: (left) EEC inside medium jets with $p_T^{\rm med} \in [170, 208]$ GeV (blue line), correspondent to vacuum jets with $p_T^{\rm vac} \in [200, 240]$ by the $Q_{\rm AA}$ method (also displayed in black line). Solid lides correspond to hadron level results, and dashed lines to parton level. Error bars are statistical only. **(right)** Ratio between the EEC at parton and hadron level, for vacuum (dark blue line) and medium (dark green line) jets.

We can also check the impact of the medium on the ratios $\rm R_{EC}^{[3,2]}$ - these are presented in Figure 5.10. It is observed that there is an enhancement of the ratio up to the intermediate/higher R_L scales, further approaching the vacuum result at very high scales. This result truly evidences that most changes of the correlators in medium jets are predominant in the transition-partonic scale, motivating a detailed analysis in this regime.

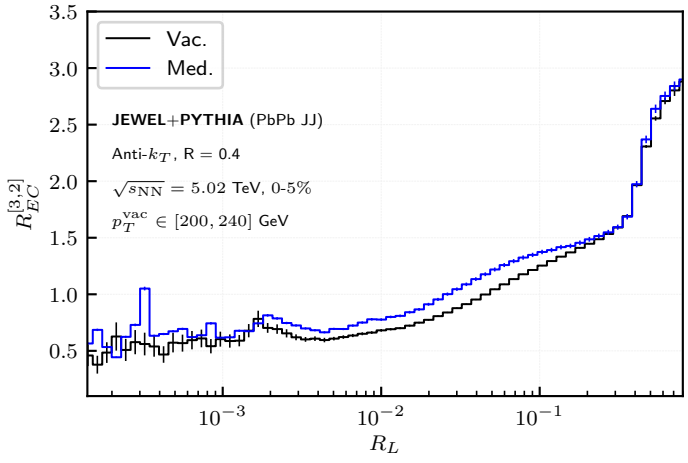

Figure 5.10: Ratios $\rm R_{EC}^{[3,2]}$ inside medium jets with $p_T^{\rm med} \in [170, 208]$ GeV (blue line), correspondent to vacuum jets with $p_T^{\rm vac} \in [200, 240]$ by the $Q_{\rm AA}$ method (also displayed in black line), using simulated data from JEWEL.

Turning back to the EEC, both at parton and hadron level, the horizontal shift of the peak stands as the most noticeable and interesting difference. The rest of this chapter is going to be spent analyzing this effect.

It would be natural to associate this shift to the same as observed in Figure 5.4, where the effect arises from the change in p_T-window. In that case, however, a similar shift is verified for vacuum jets with *higher* momentum, whereas in this case, the comparison is being made with vacuum jets and its medium-modified counterparts, which have *lower* momentum. The p_T-window shift effect is only meaningful when comparing jets that had the same evolution conditions, which is not the case here.

One could also associate such effects with a deviation arising from using the Q_{AA} method, which is approximate and could yield unfaithful p_T-windows. In order to exclude this hypothesis, we will, from now on, analyze Z+jet events. Figure 5.11 shows the EEC in Z+jet events, with $p_T^Z = (500 \pm 5)$ GeV, using JEWEL's default settings. The results are consistent with what was obtained with dijet events, using the Q_{AA} method, and the shift is still clearly visible.

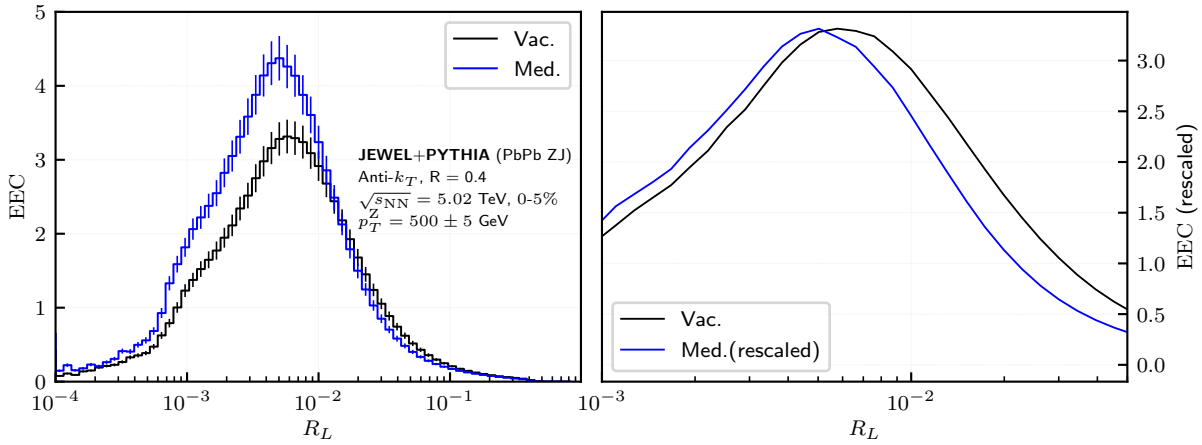

Figure 5.11: (left) EEC inside medium (blue line) and vacuum (black line) jets, associated with a with $p_T^Z = 500 \pm 5$ GeV, using simulated data from JEWEL. Error bars are statistical only. **(right)** Rescaled EEC, in order for the maximum of EEC in vacuum to coincide with the maximum the EEC in medium. Error bars are omitted for visualization purposes.

This shift could also be interpreted in terms of QCD phases and the hypothesis that the formation time is given by $\tau \simeq 1/(p_T R_L^2)$ [47], where p_T is the average jet particle momentum, from where one could associate the effect to possible delay on the hadronization time in jets that evolve in the QGP medium. The average particle momentum does not change significatively with the medium interactions, allowing us to focus mainly on the shift of R_L.

Hadronization scales in medium are associated with the critical temperature T_c of the QGP; a natural test would therefore be to analyze the behavior of the EEC's horizontal shift with T_c.

Figure 5.12 displays the results for the critical temperatures $T_c \in \{0.17,\ 0.34,\ 0.50\}$ GeV, with the default initial temperature $T_i = 0.55$ GeV. A reduction of the shift is apparent when the critical temperatures increase, which is an expected effect: closer critical temperatures to the initial approach the vacuum results. This is also compatible with the idea that higher critical temperatures reduce the time it takes for hadronization to begin, as previously pointed out.

Changing T_c, while keeping T_i fixed, not only should change the hadronization scale, but also the amount of quenching jets go through. The previous test is insufficient in order to conclude that the shift arises from the hadronization scale, given the mixture of both effects.

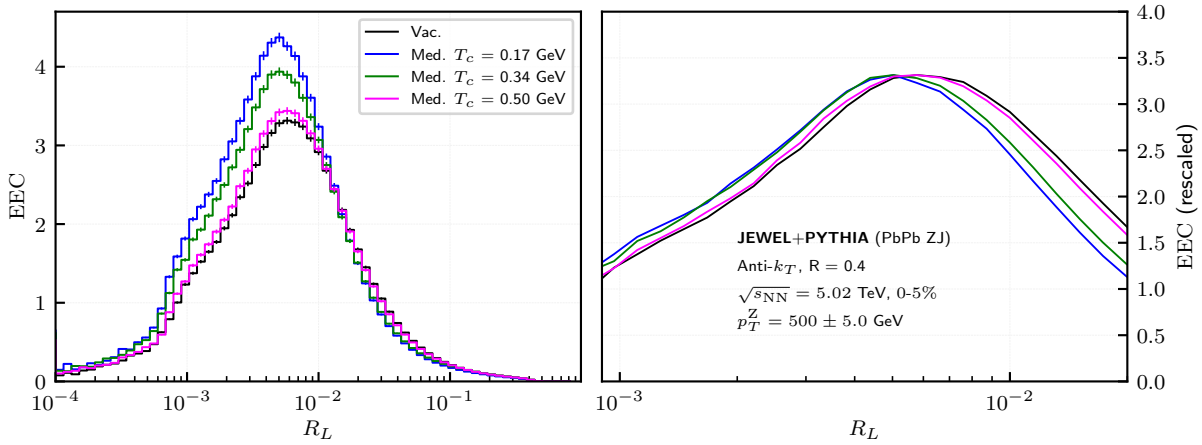

Figure 5.12: **(left)** EEC inside medium and vacuum (black line) jets, associated with a with $p_T^Z = 500 \pm 5$ GeV, for various critical temperature configurations: $T_c = 0.17$ GeV (blue line), $T_c = 0.34$ GeV (green line) and $T_c = 0.50$ GeV (magenta line), all with an initial temperature of $T_i = 0.55$ GeV, using simulated data from JEWEL. Error bars are statistical only and were reduced by a factor of 5 for visualization purposes. **(right)** Rescaled EEC, in order for all the EEC maxima to coincide. Error bars are omitted for visualization purposes.

In the proceeding test, we will analyze the settings $(T_i, T_c) = (0.55, 0.17)$ GeV (default setting), $(T_i, T_c) = (0.55, 0.50)$ GeV, and a new setting with an equivalent amount of quenching of the latter, but with $T_c = 0.17$ GeV (corresponding the same hadronization scale as the default setting). We need to compute T_i for this setting. The temperature of the plasma in the Bjorken model used in JEWEL, in terms of the time τ, is given by [50]

$$T(\tau) = T_i \left(\frac{\tau}{\tau_i}\right)^{-1/3}, \tag{5.5}$$

from where we obtain that the time τ_f it takes for the plasma to freeze out is

$$\tau_f = \tau_i \left(\frac{T_i}{T_c}\right)^3. \tag{5.6}$$

The amount of quenching Q can by estimated by

$$Q = \int_{\tau_i}^{\tau_f} T(\tau) \mathrm{d}\tau, \tag{5.7}$$

giving, using Eqs. (5.5) and (5.6),

$$Q = \frac{3}{2} T_i \tau_i \left[\left(\frac{T_i}{T_c}\right)^2 - 1\right]. \tag{5.8}$$

In our generation settings, we are always using the same value of $\tau_i = 0.60$ GeV. From this calculation, equalizing the amounts of quenching Q, the medium configuration with $T_c = 0.17$ GeV and the same Q of $(T_i, T_c) = (0.55, 0.50)$ GeV must have an initial temperature of $T_i = 0.22$ GeV. In Figure 5.13, the results for all these configurations are displayed, where all the EEC were rescaled to coincide the value of the maxima.

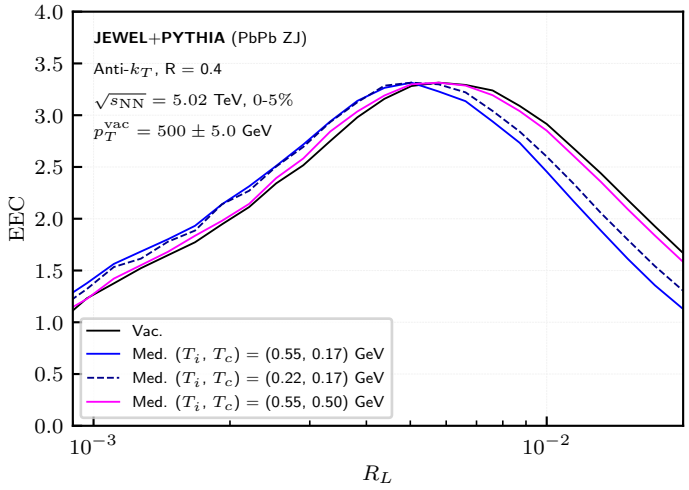

Figure 5.13: Rescaled EEC, in order for all the EEC maxima to coincide, for the vacuum (black line) and the medium configurations: $(T_i, T_c) = (0.55, 0.17)$ GeV (solid blue line), $(T_i, T_c) = (0.22, 0.17)$ GeV (dashed blue line) and $(T_i, T_c) = (0.55, 0.50)$ GeV (magenta line). Error bars are omitted for visualization purposes.

A small enhancement of the rescaled EEC in $R_L > R_{\mathrm{peak}}$ of this new configuration, in comparison with the default setting, is verified, which could be interpreted as a small shift. Even in such case, it is still very far from matching the results from $(T_i, T_c) = (0.55, 0.50)$ GeV, and would constitute a slight deviation that is very likely to be within the uncertainty of the method (e.g. different widths of the jet p_T window). However, it is still remarkable how a short-lived medium produces such a significant shift, allowing to safely state that most of the shift effect is not due to quenching.

Another evidence to support this claim, and that the shift could be associated with a hadronization delay, are the results for the EEC in HYBRID. In this generator, the parton showering "length" does not take into account how long the medium lives: as stated in Chapter 2, showering is similar to vacuum and energy loss is applied parton by parton in the whole shower history. Using the Q_{AA} method, which in JEWEL yielded similar behaviors to Z+jet events' results, we display in Figure 5.14 the EEC for vacuum jets with $p_T \in [200, 240]$ GeV and its medium counterpart, with $p_T \in [171, 209]$ GeV, in HYBRID.

These results show that the peaks coincide for both cases, proving at least that the horizontal shifts are a behaviour related to some feature exclusive to JEWEL, which is compatible with hadronization delay hypothesis.

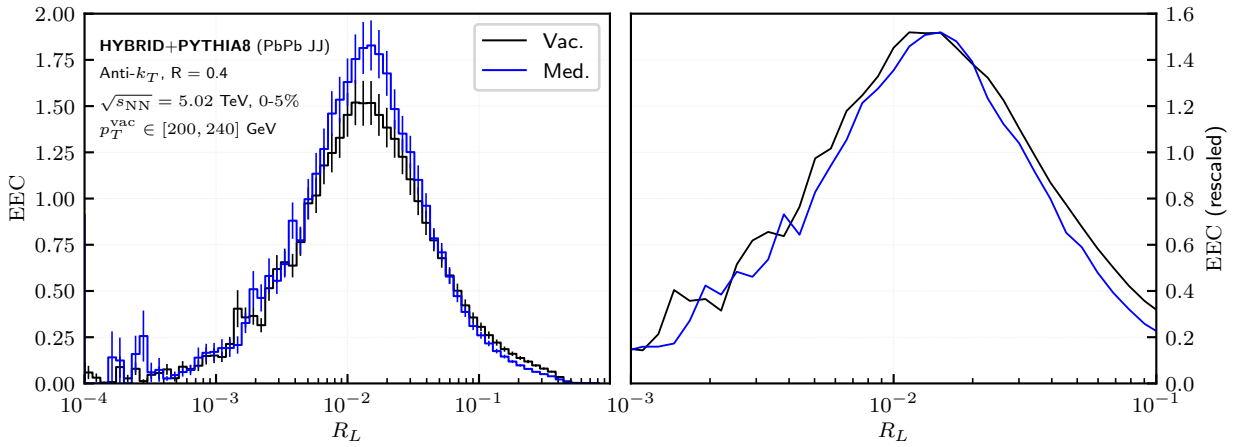

Figure 5.14: (left) EEC inside medium jets with $p_T^{med} \in [171, 209]$ GeV (blue line), correspondent to vacuum jets with $p_T^{vac} \in [200, 240]$ by the Q_{AA} method (also displayed in black line), using simulated data from HYBRID. Error bars are statistical only. **(right)** Rescaled EEC, in order for all the EEC maxima to coincide. Error bars are omitted for visualization purposes.

5.4 Summary

In this chapter, we have analyzed the EEC and ratios in vacuum and the modifications induced by medium on these functions.

Vacuum results have shown that the EEC displays different signatures to each QCD phase, dictated by the different regimes of the scale R_L. This was reinforced by results at parton level, where a suppression of the hadronic and transition phase was observed. The ratios have shown a linear behavior of the correlation with $\log(R_L)$.

The corresponding medium results have mainly displayed a shift of the correlation with respect to their vacuum counterparts. We have associated this shift to a possible delay of the hadronization, which motivated the analysis of medium results with different critical temperatures. The obtained results have shown to be compatible with this idea. Future work will be performed in order to analyze if this shifting effect is truly due to hadronization scales.

Chapter 6

Medium Response Results

In this chapter, we aim to study the impacts of medium response on the EEC. We begin by introducing the methodology and general considerations in order to properly deal with medium response in JEWEL and HYBRID, focusing on the context of this observable. Then, the results for two-point for correlations in both models are presented, followed by weighted, higher-point correlations and ratios.

Medium response is shown to have impact on the higher scales of the correlation function. This impact changes when considering weighted correlations; we have verified that it enhances for a power $n = 0.5$ and suppresses for a power $n = 2$.

6.1 Methodology and prior considerations

Inside a reconstructed medium jet, two classes of particle compositions are expected to exist: those arising from the QCD showering, which succeeds the hard scattering process, and those coming from the medium response. In nature, these classes are indistinguishable, given that both simply constitute hadrons. It is, however, possible to infer the impact of each class, through theoretical studies or using MC event generators whose results are shown to be compatible with experiment. In this chapter, we will make use of MC event generators, namely JEWEL and HYBRID, to study the effects of medium response on EECs.

In HYBRID, these classes are completely distinguishable and identifiable, given that this generator's mechanism allows to assign a different label for each kind, allowing to analyze its effects on EECs by selecting the particles of interest contributing to the correlation. We will adopt this method for this generator. In JEWEL, however, this is not possible at hadron level, since, as pointed out in Chapter 2, the medium recoiled partons hadronize within the whole jet, making it impossible to label a hadron according to its nature. The impact of medium response is, hence, inferred by comparing events with and without response. In this section, a method to properly associate medium jets from events with response to medium jets from events without this effect, in JEWEL, will be proposed.

The addition of medium response particle inside a jet increases its transverse momentum, p_T. This is a *migration* effect, as the one discussed in the previous chapter. We can try to incorporate the ideas used to compare vacuum and medium jets to the context of comparing jets with and without response.

In Chapter 5, two methods to deal with migration were used: the Q_{AA} method, used to determine average correspondent p_T-windows, and the method where the p_T of the tagged Z-boson in Z+jet events is fixed. Even though the latter would probably be the most reliable, it is observed that response contributions are relatively *uniform* along jets, i.e., it is not expected for a narrow range (p_T-window) of jets without response to be associated with a wider range of jets with response. A similar method to the Q_{AA} in this context should be, therefore, more accurate than when it is used to compare vacuum and medium jets. A further motivation to focus on this method was already previously pointed out: its possible application on dijet events. For completeness, however, a result using Z+jet events will be also presented.

Given these considerations, we propose to use an adaptation of the Q_{AA} method in JEWEL dijet events, comparing medium events with and without response instead of comparing vacuum and medium. This is achieved using a new observable $\bar{Q}_{\mathrm{AA}}$, defined by

$$\bar{Q}_{\mathrm{AA}} \overset{\mathrm{def}}{=} \left.\frac{p_T^{\mathrm{wo/resp}}}{p_T^{\mathrm{w/resp}}}\right|_{\Sigma^{\mathrm{eff}}}, \tag{6.1}$$

with a similar methodology to the one outlined in Chapter 5. In this case, p_T^{quant} will correspond to the statistically equivalent jet with response momentum of a jet without response. Figure 6.1 displays the effective cross-section, Σ_{eff}, and the correspondent $\bar{Q}_{\mathrm{AA}}$ in JEWEL, using the default medium parameters, in the quantile momentum interval $p_T^{\mathrm{quant}} \in [150, 300]$ GeV.

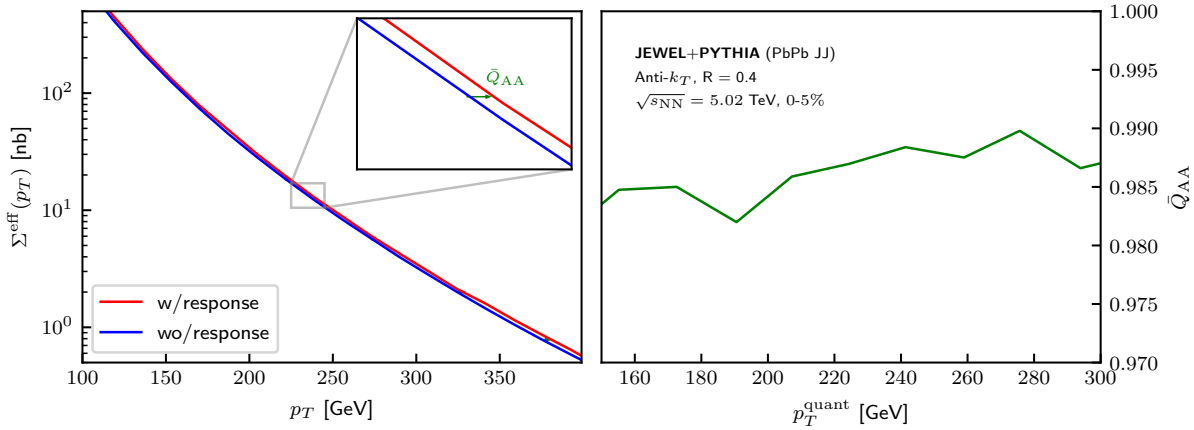

Figure 6.1: (left) Cumulative cross-section as a function of p_T, for medium jets with response (red line) and without (blue line) jets. Inside the zoomed-in box, the arrow indicates that the $\bar{Q}_{\mathrm{AA}}$ is computed by taking the ratio between the p_T of jets with and without response with the same Σ_{eff}. **(right)** The corresponding $\bar{Q}_{\mathrm{AA}}$, as a function of the quantile momentum, p_T^{quant}.

From events in JEWEL, we will be mainly studying jets (with response) in the interval $p_T^{\mathrm{jet}} \in [200, 240]$ GeV. Using this method, the non-response counterpart would correspond to jets in $[196, 237]$ GeV.

It is important to note that these are jets that went through different reclustering processes. In JEWEL, it turns out that the recoils distribution is such that, after reconstruction, the radial momentum distribution suffers a slight shift on the hard core region, as evidenced with the plots in Figure 6.2 with

the distribution $\mathrm{d}p_T/\mathrm{d}r$ and the cumulative momentum inside the jet, defined by

$$p_T^{\text{cumulative}}(r) = \int_0^r \frac{\mathrm{d}p_T}{\mathrm{d}r'}\mathrm{d}r', \tag{6.2}$$

where r is the geometric distance from the axis.

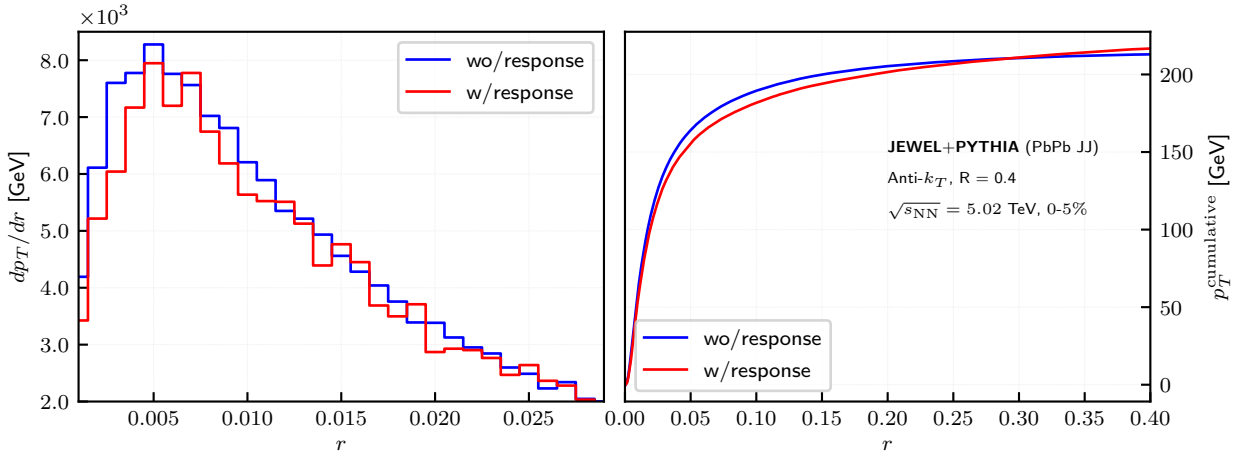

Figure 6.2: (left) Distribution dp_T/dr inside a jet with (red line) and without (blue line) response. (right) Corresponding cumulative momentum, $p_T^{\text{cumulative}}(r)$, inside the jet, as a function of the geometric distance r, using jets with $p_T \in [200, 240]$ GeV.

The EEC is a function that is computed using distances. Given what we have just pointed out, when comparing jets from events with and without response, it is expected to observe a modification, coming from the shift on the momentum distribution. This will be considered a systematic deviation in results from JEWEL, arising from the comparison between jets from different events (with and without response), that went through different clustering processes.

6.2 2-point correlations

From Eq. (3.19), and given that medium response is essentially an *addition* of particles, one expects that the EEC inside a jet with medium response particles splits into

$$\mathrm{EEC}(R_L) = \mathrm{EEC}_{\text{no-resp.}}(R_L) + \mathrm{EEC}_{\text{resp.}}(R_L), \tag{6.3}$$

where $\mathrm{EEC}_{\text{no-resp.}}(R_L)$ corresponds to the contribution from the jet particles (i.e. non-response) and $\mathrm{EEC}_{\text{response}}(R_L)$ the term corresponding to medium response impacts. The latter contribution can also be split in two: one arising from the correlations of the regular jet particles with the response particles (a *cross term*) and the other coming purely from correlations between response particles, i.e.,

$$\mathrm{EEC}_{\text{resp.}}(R_L) = \mathrm{EEC}_{\text{cross}}(R_L) + \mathrm{EEC}_{\text{only-resp.}}(R_L). \tag{6.4}$$

Eqs. (6.3) and (6.4) should also apply when considering the logarithmic correlator, $\mathrm{EEC}_{\ln}(R_L)$ and the weighted correlations, $\mathrm{E^nEC}(R_L)$.

In HYBRID, Eqs. (6.3) and (6.4) are expected to be completely verified, given the methodology adopted for this generator; in JEWEL, some slight differences are expected for lower distances, given the systematic deviation arising from comparing different jets.

We aim to analyze the impact of the medium response on the EEC, i.e., the term $\mathrm{EEC}_{\mathrm{resp.}}(R_L)$. In JEWEL, however, the comparison is being made between jets from events with response and events without, and the latter jets possess a lower p_T by a factor of $\bar{Q}_{\mathrm{AA}}$. It is necessary to have the same p_T in order for Eq. (6.3) to make sense, given that our physical objects of interest are jets with response; in terms of the EEC, this can be achieved by rescaling the $p_T^{\mathrm{jet}} \to \bar{Q}_{\mathrm{AA}} p_T^{\mathrm{jet}}$ on jets from events without response.

Figures 6.3a and 6.3b show the results for the EEC and the ratio between the cases with and without response, respectively in JEWEL and HYBRID.

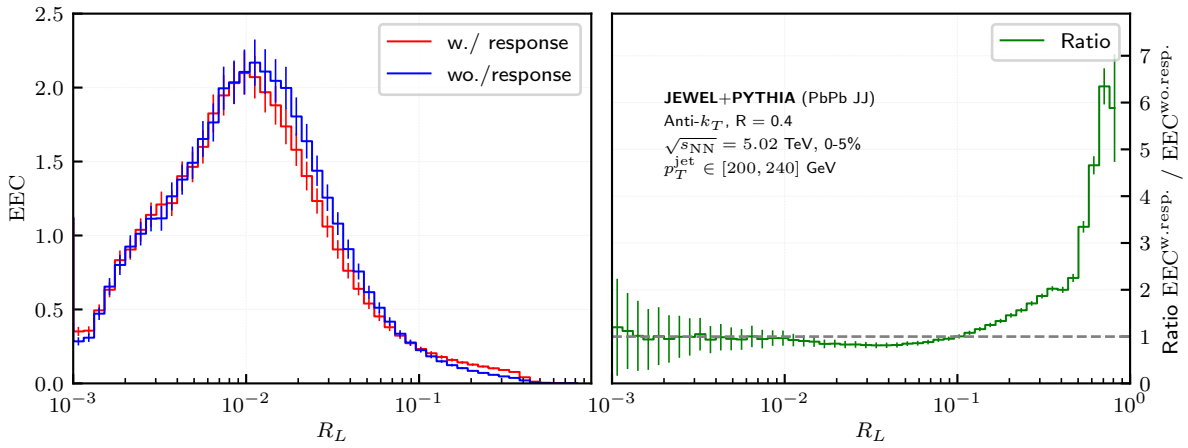

(a) JEWEL results.

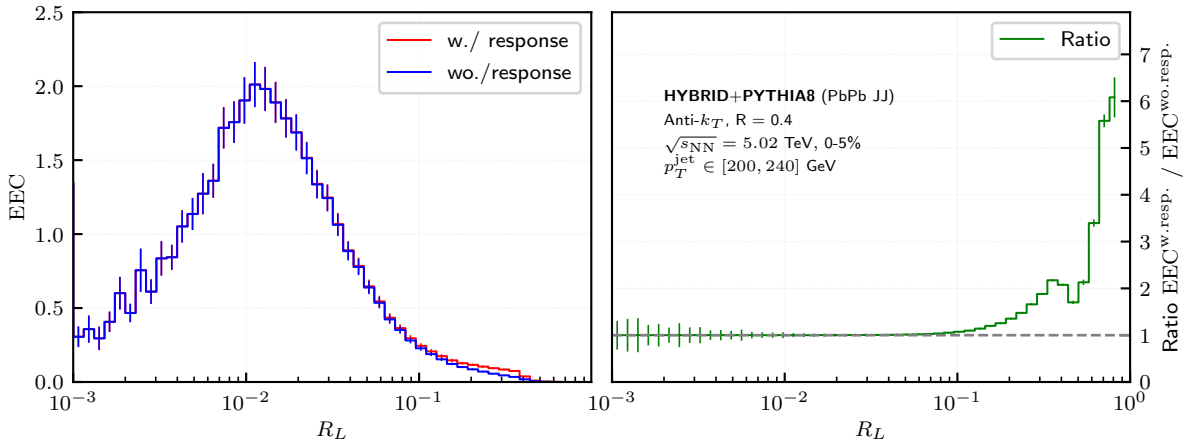

(b) HYBRID results.

Figure 6.3: Results for the medium response impacts on the EEC, for jets with $p_T^{\mathrm{jet}} \in [200, 240]$ GeV in **(a)** JEWEL and **(b)** HYBRID. For each generator, on the **(left)**, the EEC is displayed in the cases of with and without response, and on the **(right)**, the corresponding ratio between each case.

Evidenced from these results, medium response is observed to impact the EEC on the higher R_L scales, even though in JEWEL, a small suppression is observed at lower R_L, which is compatible with the observed deviation. The increase of the EEC on higher R_L, for both generators, is due to the distribution of medium response particles within the jet, and has nothing to do with the QCD phases interpretation, used in the previous chapter. With this effect, the interpretation that high R_L scales mainly imprints the partonic phase is no longer valid, given the significant contribution of medium response in this region.

Globally, medium response effects could be hard to identify in EECs, given that these signatures are not that visible in the bigger picture and the ratios displayed in Figures 6.3a and 6.3b, which help to identify response signatures, are just an artifact only determinable in the context of MC event generators. Naively, without taking the ratio in consideration, one could even state that the EEC is insensitive to the medium response. However, these signatures are quite noticeable for the $\mathrm{EEC_{ln}}$, where the correlations in higher R_L scales are enhanced, as displayed in Figure 6.4. For this observable, in both generators, the QGP response signature is identifiable for $R_L > 0.1$, with the systematic deviation in JEWEL results for lower R_L scales.

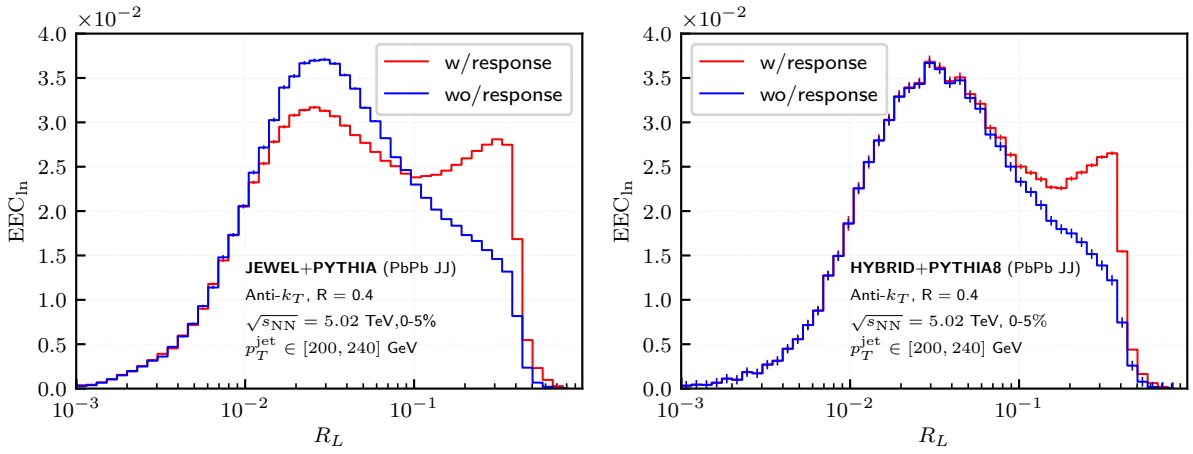

(a) JEWEL results. **(b)** HYBRID results.

Figure 6.4: Results for the medium response impacts on the $\mathrm{EEC_{ln}}$, for jets with $p_T^{\mathrm{jet}} \in [200, 240]$ GeV in **(a)** JEWEL and **(b)** HYBRID. For each generator, the EEC is displayed in the cases of with and without response

The results for both generators in the higher scales are remarkably similar, even though their medium response's mechanisms are completely different, increasing the robustness of the results.

Using HYBRID, it is possible to analyse each one of the terms in Eqs. (6.3) and (6.4) in the high R_L scales by manually selecting the particles of interest to fill the EEC histogram, which we assume to also approximately hold in JEWEL due to the similarities of both signatures.

Figures 6.5a and 6.5b display each contribution type for the regular and logarithmic correlations, respectively. These results show that most response contributions arise from the cross term; as evidenced with the figures on the right, the cross term is $\sim$ 20-30 times greater than the only-response contribution. A considerable fraction of the cross term comes from the correlation between response particles (distributed on the whole jet) and jet hard core particles, hence the significant decrease of the correlation when $R_L > R_{\mathrm{jet}} = 0.4$, given that particles from the hard core cannot contribute more in this regime.

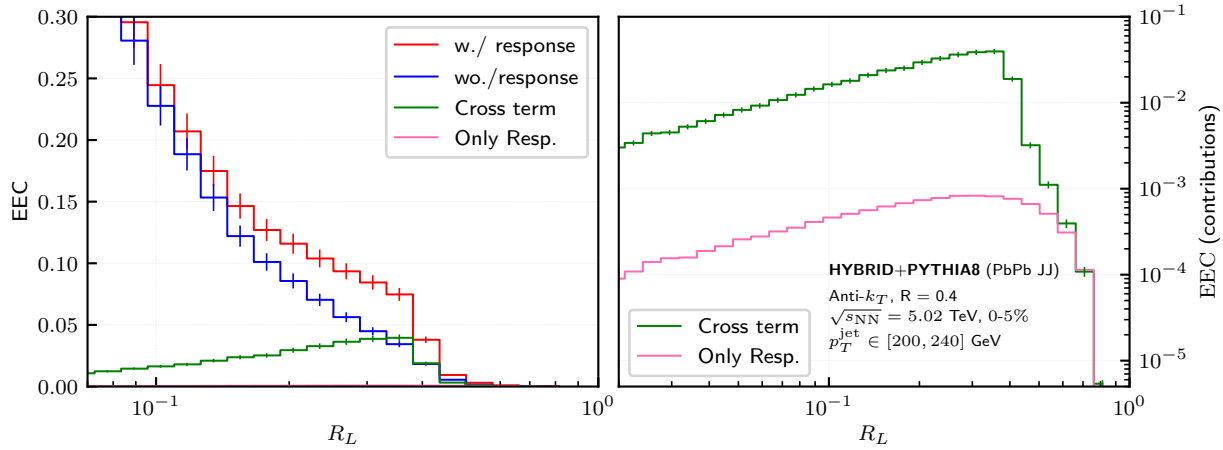

(a) Regular correlation contributions.

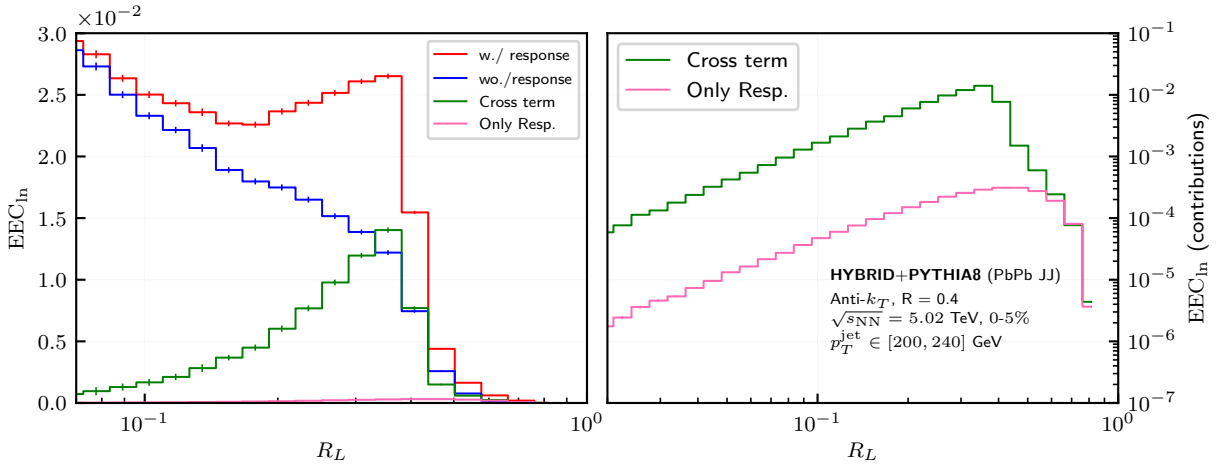

(b) Logarithmic correlation contributions.

Figure 6.5: Cross and only-response terms contribution to (a) the EEC and (b) the EEC_{ln}, using HYBRID. For each correlation function, on the **(right)**, each contribution, along the total with and without response EECs, is displayed. On the **(left)**, the cross and only-response terms are displayed in log scale.

The other (far smaller) fraction comes from correlations between response particles and jet particles on the periphery.

It is also possible to analyze the dependence of these terms with the jet momentum. In order to do that, we will study the ratio between the correlation with and without response; the goal is to analyze the relative impact of response particles compared to the correlations of jets without response. Using jets in p_T-windows $[120, 160]$ GeV, $[200, 240]$ GeV and $[280, 320]$ GeV, we display in Figure 6.6 the results for the cross and only response terms.

The cross term contribution, relative to the correlation without response, is shown to be approximately the same for different jet transverse momenta, while the only response terms tend to decrease with the increase of the momentum. This behavior is compatible with the observations that the average momentum of jet particles increases with jet momentum, while the momentum of response particles are approximately independent of the jet momentum. The overall impact of the response on the correlations is, therefore, expected to be similar for jets with different transverse momentum, which is mainly dictated by the cross

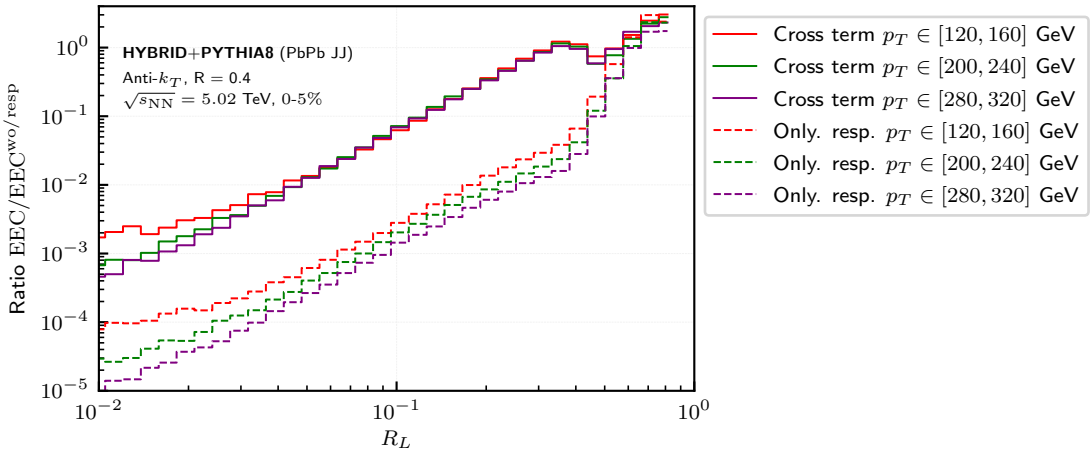

Figure 6.6: Cross and only-response terms, divided by the total EEC without response, for different p_T-windows: $p_T \in [120, 160]$ GeV, $p_T \in [200, 240]$ GeV and $p_T \in [280, 320]$ GeV, using HYBRID.

terms, allowing for the response signatures to be detectable for any jet momentum.

For completeness, we display in Figure 6.7 results for Z+jet events in JEWEL, using $p_T^Z = 500 \pm 5$ GeV. The signatures are shown to be similar to the previous case of dijet events. The displacement of the region where the systematic deviation occurs is due to the shift observed when considering different jet p_T windows, as pointed out in the previous chapter (these are jets with $p_T \sim 400$ GeV). Moreover, we still observe the medium response signatures at higher R_L scales, even though these are jets with a substantially higher p_T, corroborating the previous statement that medium response signatures are always identifiable due to the cross term.

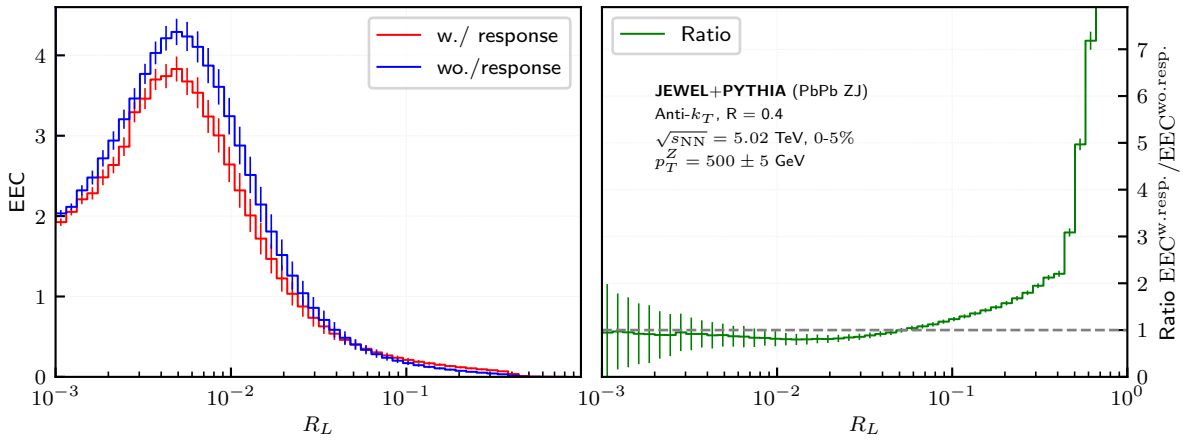

Figure 6.7: Results for the medium response impacts on the EEC, for jets with $p_T^Z = 500 \pm 5$ GeV in JEWEL. On the **(left)**, the EEC is displayed in the cases of with and without response, and on the **(right)**, the corresponding ratio between each case.

6.3 Weighted correlations

Response particles are, in general, considerably softer than the average jet particle. This motivates the analysis of weighted correlation functions, $\mathrm{E}^n\mathrm{EC}$, where the values of the exponent n are expected control the overall impact of particles of each kind.

In the case where $n = 0.5$, we expect to enhance the effects of low momentum particles on the correlation function (and reduce the impact of high-momentum particles). This is observed on the results displayed in Figure 6.8, where we get a significant impact of the medium response on the correlation functions, for both generators, specially for the logarithmic correlations. On the other hand, $n = 2$

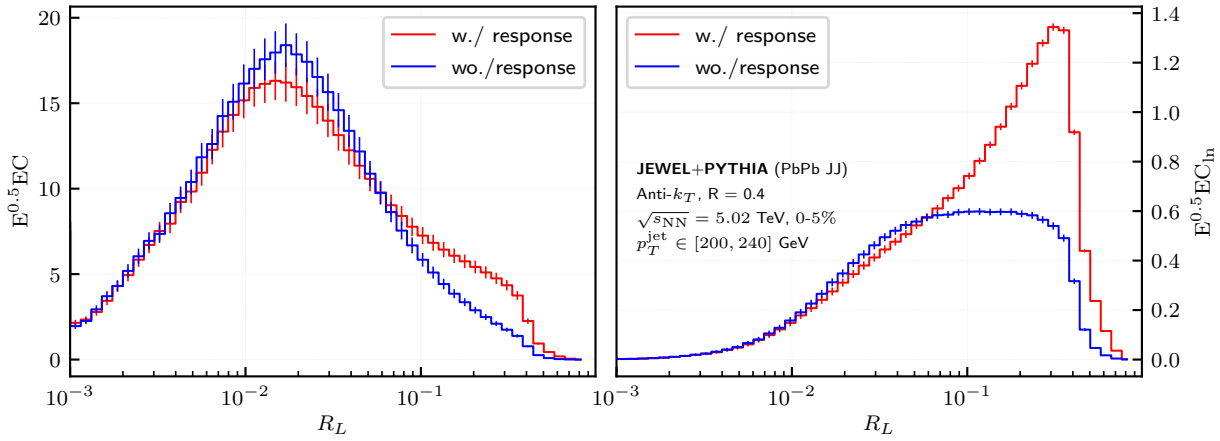

(a) JEWEL results.

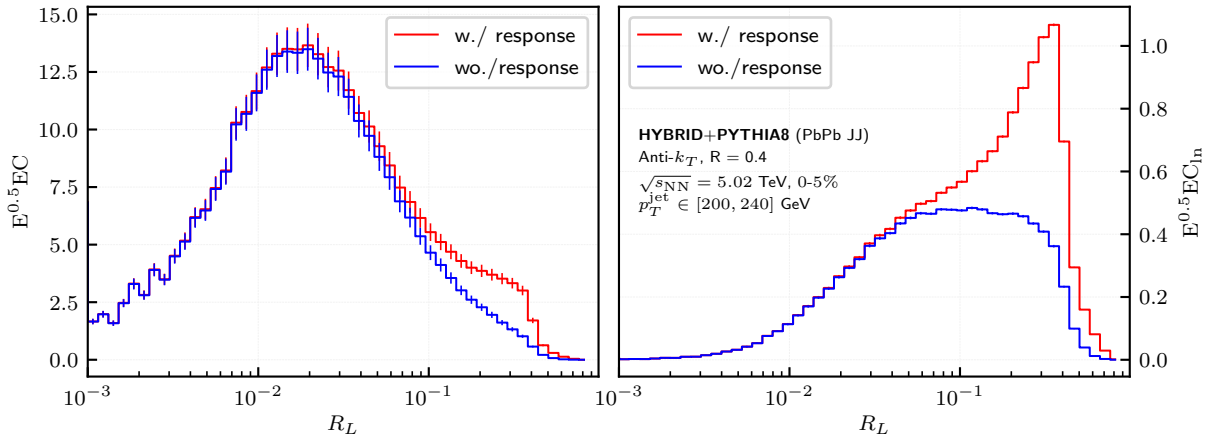

(b) HYBRID results.

Figure 6.8: Results for the medium response impacts on the $\mathrm{E}^{0.5}\mathrm{EC}$, for jets with $p_T^{\mathrm{jet}} \in [200, 240]$ GeV in JEWEL (a) and HYBRID (b). For each generator, on the **(left)**, the $\mathrm{E}^{0.5}\mathrm{EC}$ is displayed in the cases of with and without response, and on the **(right)**, the corresponding ratio between each case.

should enhance high-momentum particles and suppress those with low momentum, i.e., suppress response contributions. Results in Figure 6.9 show exactly this effect. In this case, the response contributions are barely detectable, even in the logarithmic correlation. This could be an interesting observable to study, given its insensitivity to medium response, which reduces the uncertainties associated with this effect.

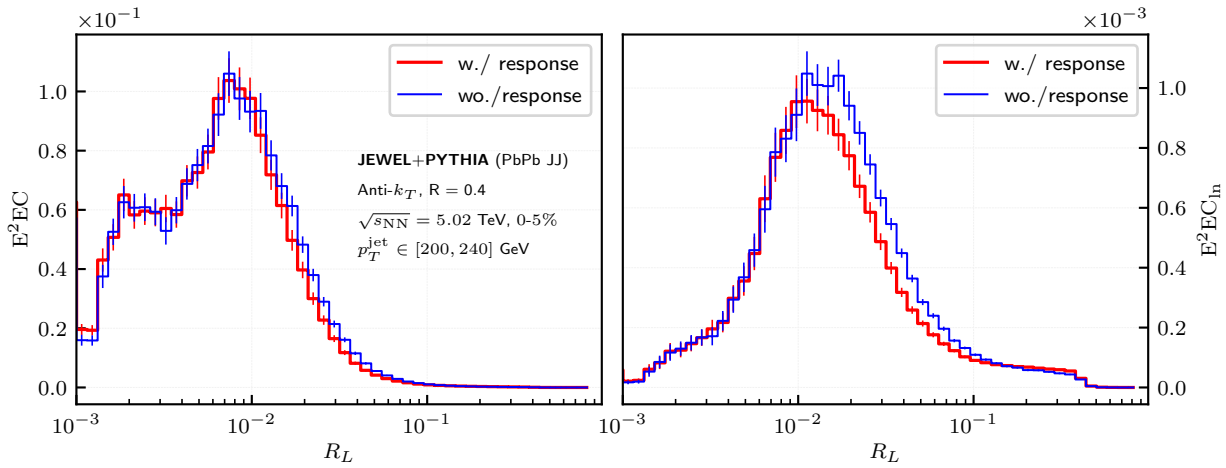

(a) JEWEL results.

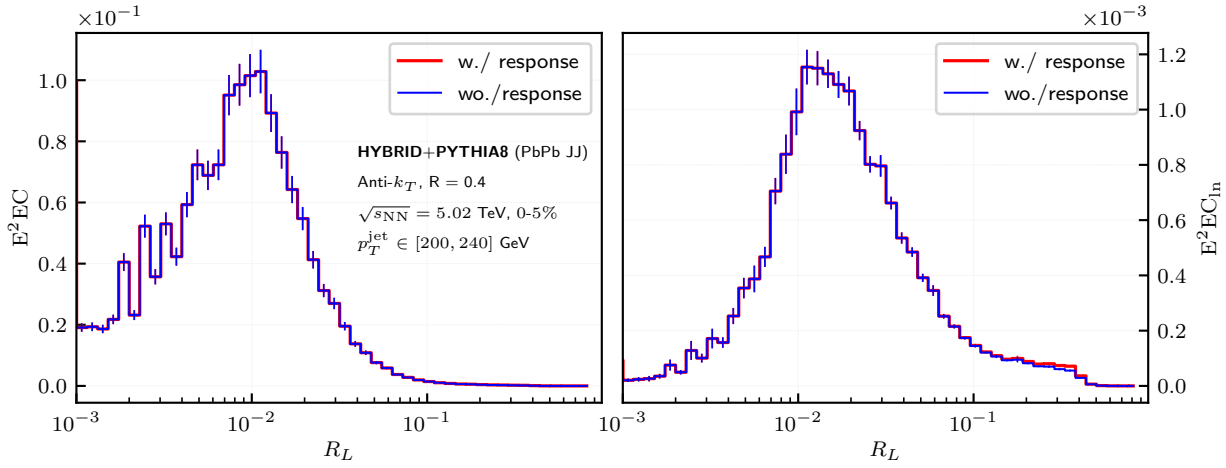

(b) HYBRID results.

Figure 6.9: Results for the medium response impacts on the $\mathrm{E}^2\mathrm{EC}$, for jets with $p_T^{\mathrm{jet}} \in [200, 240]$ GeV in JEWEL (a) and HYBRID (b). For each generator, on the **(left)**, the $\mathrm{E}^{0.5}\mathrm{EC}$is displayed in the cases of with and without response, and on the **(right)**, the corresponding ratio between each cases.

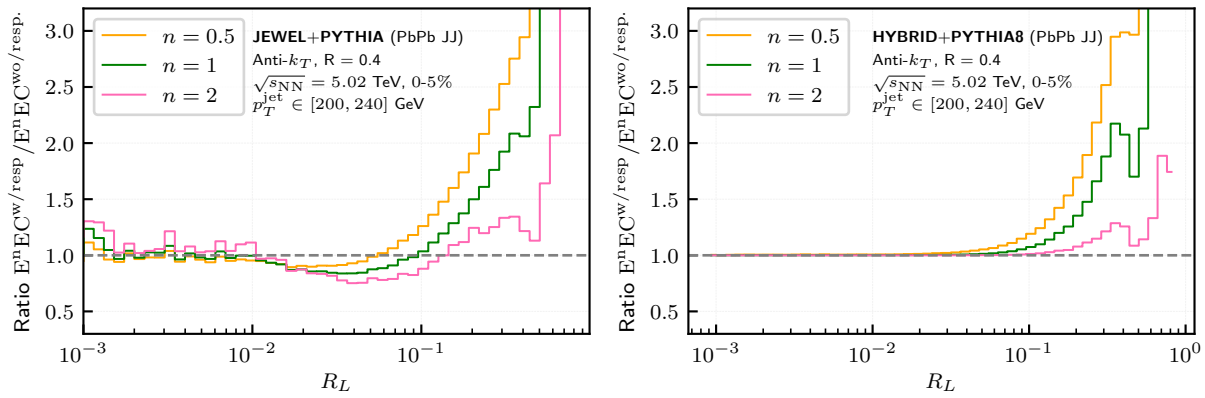

(a) JEWEL results.

(b) HYBRID results.

Figure 6.10: Ratios between the $\mathrm{E}^{\mathrm{n}}\mathrm{EC}$ in jets with and without response, for $p_T^{\mathrm{jets}} \in [200, 240]$ GeV in JEWEL (a) and HYBRID (b), in the cases $n = 0.5, 1, 2$.

In Figure 6.10, the ratios between the weighted correlations with and without response are displayed, for $n = 0.5$, $n = 1$ (the case of the previous section) and $n = 2$. Not only the response contributions change in the bigger picture, but so does the relative impact of the medium response with respect to the case without response.

The addition rules in Eqs. (6.3) and (6.4) are also valid in the case of weighted correlations, for each n. The dependence of the cross and only-response terms on n can be analyzed, as Figure 6.11 shows for $n = 0.5, 1, 2$ relative to results without response.

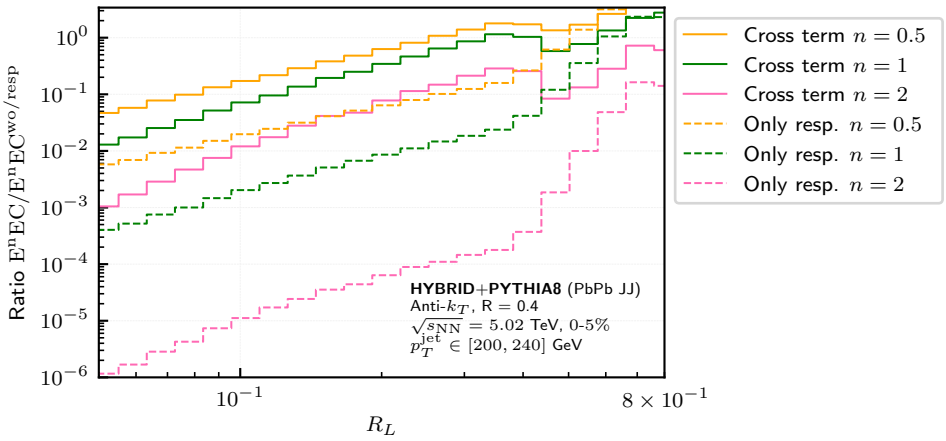

Figure 6.11: Weighted correlations' cross and only-response terms, for each case $n = 0.5, 1, 2$,using HYBRID.

Both cross and only-response terms decrease with the increase of n, as expected from the previous results, but it is also remarkable that only-response terms become less important with n, when compared with the cross terms: for $n = 0.5$, cross terms are ~ 10 times greater than only-response, while for $n = 2$, it's a difference of about $\sim 10^3$ times.

6.4 Ratios

We will now analyze the impact of medium response in ratios. In particular, we will be studying the effects on the ratio $R_{EC}^{[3,2]}$. In figure 6.12, the results for this case are presented.

Both generators agree on the results at higher R_L scales, where a suppression of the ratio is observed; such modification is compatible with the results that medium response predominantly impacts the correlators in this region. In JEWEL, the ratios for lower scales approximately coincide for the cases with and without response, while in HYBRID, without response ratios are slightly higher than with response along the whole R_L domain. This discrepancy can be justified by the deviation on the lower scales in JEWEL, which also impacts the ratios in this region.

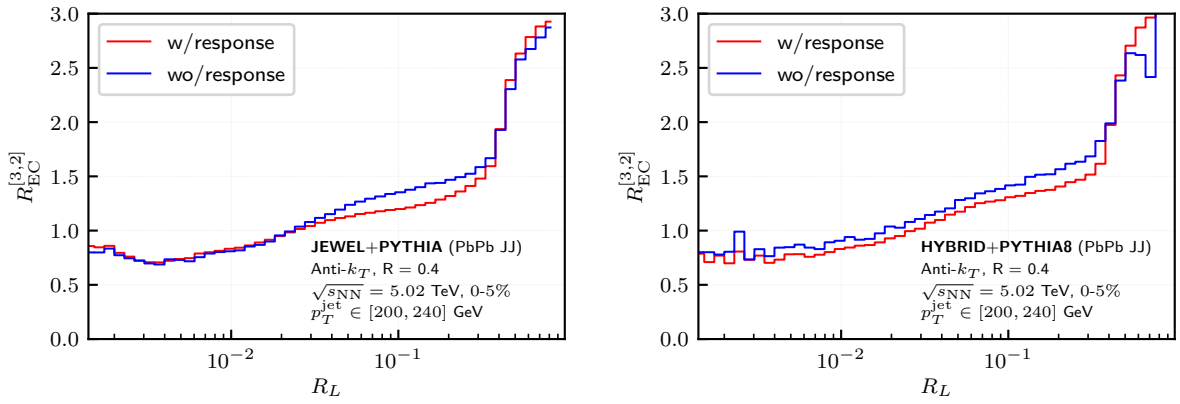

(a) JEWEL results.

(b) HYBRID results.

Figure 6.12: Results for the medium response impacts on the ratio $R_{EC}^{[3,2]}$, for jets with $p_T^{jet} \in [200, 240]$ GeV in JEWEL (a) and HYBRID (b). For each generator, the $R_{EC}^{[3,2]}$ is displayed in the cases of with (red) and without (blue) response

6.5 Summary

Throughout this chapter, medium response effects on the EEC, EEC_{ln}, E^nEC and ratios were studied in detail, in JEWEL and HYBRID.

We began by analyzing the impacts on EEC and EEC_{ln}, where an enhancement on the higher scales was observed in both generators. The EEC_{ln} evidenced that effect more clearly. The term on the correlation functions arising from medium response can be split in cross and only-response terms, which were analyzed using HYBRID. We have shown that the cross term is dominant over the only-response one, and that the relative impact of the cross term (to the correlations without response) are the same for different jet p_T, while the only-response term decreases.

These results were proceeded by the weighted correlations, E^nEC; an enhancement of the response signatures was observed for $n = 0.5$, and a suppression for $n = 2$, both for the absolute correlation and for the ratio between with and without response cases.

Finally, the ratio was analyzed, and both generators agreed on a suppression of the ratio at higher R_L scales.

Chapter 7

Conclusions

In this work, the behavior of energy correlators inside jets in pp and PbPb collisions was studied, with the main goal to analyze the impact of the QGP medium on these observables. Results were obtained using simulated data from JEWEL and HYBRID.

First, energy-energy correlations (EEC) inside jets from pp collisions, which evolved in vacuum, were analyzed. We have identified the different QCD phases imprinted in this function: hadronic for lower scales, transition for intermediate scales, characterized by a peak of the distribution, and partonic for higher scales. Then, we moved onto jets from PbPb collisions, without taking medium response into account. In JEWEL, in comparison with the vacuum, the EEC revealed a shift of its peak, which we have hypothesized to be related to a hadronization delay. An extensive study of this shift was performed by analyzing different critical temperatures of the medium, which are related to the hadronization scale. We have also checked that this shift is not featured in HYBRID results, where the hadronization delay is not expected to occur. All the results were compatible with this hypothesis.

Further, we have analyzed the effects of medium response on the energy correlators. The main conclusion from these results is that medium response predominantly impacts the correlation functions on the higher scales. We have stated that the EEC inside jets with medium response are split in the correlations of the non-response particles (jet particles), correlations between jet and response particles (cross-term) and correlations purely between response particles (only response term). It has been shown using HYBRID that the cross-term is dominant in the medium response contribution, allowing the signatures to be identified for any jet momentum. We have also analyzed weighted correlations, where a power n is placed in the momentum dependence of the correlator. A suppression of the medium response signatures was observed for $n = 2$ and an enhancement for $n = 0.5$.

Following this work, the most natural step will be to perform further tests in order to obtain more robust conclusions about the hadronization delay. An example of such test would be to compute the EEC in events where the parton showering in medium stops at the same scale as in the vacuum, which is currently not a functionality in JEWEL and needs to be implemented.

Bibliography

[1] S. L. Glashow. Partial-symmetries of weak interactions. *Nuclear Physics*, 22:579–588, 2 1961. ISSN 0029-5582. doi: 10.1016/0029-5582(61)90469-2.

[2] S. Weinberg. A model of leptons. *Phys. Rev. Lett.*, 19:1264–1266, Nov 1967. doi: 10.1103/PhysRevLett.19.1264. URL https://link.aps.org/doi/10.1103/PhysRevLett.19.1264.

[3] G. 't Hooft and M. Veltman. Regularization and renormalization of gauge fields. *Nuclear Physics B*, 44:189–213, 7 1972. ISSN 0550-3213. doi: 10.1016/0550-3213(72)90279-9.

[4] M. Thomson. *Modern particle physics*. Cambridge University Press, 2013.

[5] M. D. Schwartz. *Quantum Field Theory and the Standard Model*. Cambridge University Press, 3 2014. ISBN 978-1-107-03473-0, 978-1-107-03473-0.

[6] P. W. Higgs. Broken symmetries, massless particles and gauge fields. *Physics Letters*, 12:132–133, 9 1964. ISSN 0031-9163. doi: 10.1016/0031-9163(64)91136-9.

[7] P. W. Higgs. Broken symmetries and the masses of gauge bosons. *Phys. Rev. Lett.*, 13:508–509, Oct 1964. doi: 10.1103/PhysRevLett.13.508. URL https://link.aps.org/doi/10.1103/PhysRevLett.13.508.

[8] T. W. B. Kibble. Symmetry breaking in non-abelian gauge theories. *Phys. Rev.*, 155:1554–1561, Mar 1967. doi: 10.1103/PhysRev.155.1554. URL https://link.aps.org/doi/10.1103/PhysRev.155.1554.

[9] M. E. Peskin. *An introduction to quantum field theory*. CRC press, 2018.

[10] G. Aad et al. Observation of a new particle in the search for the Standard Model Higgs boson with the ATLAS detector at the LHC. *Phys. Lett. B*, 716:1–29, 2012. doi: 10.1016/j.physletb.2012.08.020.

[11] H. M. Lee. Lectures on physics beyond the standard model. *Journal of the Korean Physical Society*, 78(11):985–1017, may 2021. doi: 10.1007/s40042-021-00188-x. URL https://doi.org/10.1007%2Fs40042-021-00188-x.

[12] R. K. Ellis, W. J. Stirling, and B. R. Webber. *QCD and collider physics*. Cambridge university press, 2003.

[13] H. D. Politzer. Reliable Perturbative Results for Strong Interactions? *Phys. Rev. Lett.*, 30:1346–1349, 1973. doi: 10.1103/PhysRevLett.30.1346.

[14] D. J. Gross and F. Wilczek. Asymptotically Free Gauge Theories - I. *Phys. Rev. D*, 8:3633–3652, 1973. doi: 10.1103/PhysRevD.8.3633.

[15] B. Schwarzschild. Physics Nobel Prize Goes to Gross, Politzer, and Wilczek for Their Discovery of Asymptotic Freedom. *Physics Today*, 57(12):21–24, 12 2004. ISSN 0031-9228. doi: 10.1063/1.1878324. URL https://doi.org/10.1063/1.1878324.

[16] P. Zyla, R. Barnett, and J. Beringer. (particle data group), prog. theor. exp. phys. 2020, 083c01. 2020.

[17] M. A. Stephanov. QCD phase diagram: an overview, 2006.

[18] Feb 2021. URL https://cerncourier.com/a/quark-matter-fireballs-hashed-out-in-protvino/.

[19] J. Stirling. Theory of proton-proton collisions. URL https://www.slac.stanford.edu/econf/C060717/lec_notes/stirling_all.pdf.

[20] W. Busza, K. Rajagopal, and W. V. D. Schee. Heavy ion collisions: The big picture and the big questions. *Annual Review of Nuclear and Particle Science*, 68:339–376, 2018. ISSN 01638998. doi: 10.1146/annurev-nucl-101917-020852.

[21] R. Pasechnik and M. Šumbera. Phenomenological review on quark-gluon plasma: Concepts vs. observations. *Universe*, 3:1–64, 2017. ISSN 22181997. doi: 10.3390/universe3010007.

[22] E. Rutherford. Lxxix. the scattering of a and b particles by matter and the structure of the atom. *The London, Edinburgh, and Dublin Philosophical Magazine and Journal of Science*, 21(125):669–688, 1911. doi: 10.1080/14786440508637080. URL https://doi.org/10.1080/14786440508637080.

[23] M. Riordan. The discovery of quarks. *Science*, 256(5061):1287–1293, 1992. ISSN 00368075, 10959203. URL http://www.jstor.org/stable/2877300.

[24] T. Sjöstrand, S. Mrenna, and P. Skands. A brief introduction to PYTHIA 8.1. *Computer Physics Communications*, 178(11):852–867, jun 2008. doi: 10.1016/j.cpc.2008.01.036. URL https://doi.org/10.1016%2Fj.cpc.2008.01.036.

[25] S. Marzani, G. Soyez, and M. Spannowsky. Looking inside jets. *Lecture Notes in Physics*, 958:1–6, 2019. ISSN 00758450. doi: 10.1007/978-3-030-15709-8_1.

[26] M. Cacciari, G. P. Salam, and G. Soyez. FastJet user manual. *The European Physical Journal C*, 72(3), mar 2012. doi: 10.1140/epjc/s10052-012-1896-2. URL https://doi.org/10.1140%2Fepjc%2Fs10052-012-1896-2.

[27] M. Cacciari, G. P. Salam, and G. Soyez. The anti-kt jet clustering algorithm. *Journal of High Energy Physics*, 2008(04):063–063, apr 2008. doi: 10.1088/1126-6708/2008/04/063. URL https://doi.org/10.1088%2F1126-6708%2F2008%2F04%2F063.

[28] H. A. Andrews, L. Apolinario, R. A. Bertens, C. Bierlich, M. Cacciari, Y. Chen, Y. T. Chien, L. C. Mendez, M. Deak, D. D'Enterria, F. Dominguez, P. C. Harris, K. Kutak, Y. J. Lee, Y. Mehtar-Tani, J. Mulligan, M. Nguyen, C. Ning-Bo, D. Perepelitsa, G. Salam, M. Spousta, J. G. Milhano, K. Tywoniuk, M. V. Leeuwen, M. Verweij, V. Vila, U. A. Wiedemann, and K. C. Zapp. Novel tools and observables for jet physics in heavy-ion collisions. *Journal of Physics G: Nuclear and Particle Physics*, 47:1–26, 2020. ISSN 13616471. doi: 10.1088/1361-6471/ab7cbc.

[29] S. Basegmez, G. Bruno, L. Ceard, C. Delaere, T. Du Pree, D. Favart, L. Forthomme, J. Hollar, V. Lemaitre, J. Liao, et al. Jet momentum dependence of jet quenching in pbpb collisions at sqrt (snn)= 2.76 tev. *Physics Letters. Section B: Nuclear, Elementary Particle and High-Energy Physics*, page 176, 2012.

[30] J. Casalderrey-Solana, D. C. Gulhan, J. G. Milhano, D. Pablos, and K. Rajagopal. Angular structure of jet quenching within a hybrid strong/weak coupling model. *Journal of High Energy Physics*, 2017, 2017. ISSN 10298479. doi: 10.1007/JHEP03(2017)135. qgp response (ch4).

[31] J. G. Milhano and K. Zapp. Improved background subtraction and a fresh look at jet substructure in jewel. *The European Physical Journal C*, 82, 2022. ISSN 14346052. doi: 10.1140/epjc/s10052-022-10954-1. qgp response (intro).

[32] I. Lokhtin, L. Malinina, S. Petrushanko, A. Snigirev, I. Arsene, and K. Tywoniuk. Heavy ion event generator hydjet++ (hydrodynamics plus jets). *Computer Physics Communications*, 180(5):779–799, 2009. ISSN 0010-4655. doi: https://doi.org/10.1016/j.cpc.2008.11.015. URL https://www.sciencedirect.com/science/article/pii/S0010465508003913.

[33] K. Zapp. Jewel 2.0.0: directions for use. *The European Physical Journal C*, 74(2), feb 2014. doi: 10.1140/epjc/s10052-014-2762-1. URL https://doi.org/10.1140%2Fepjc%2Fs10052-014-2762-1.

[34] N. Armesto, L. Cunqueiro, and C. A. Salgado. Q-PYTHIA: a medium-modified implementation of final state radiation. *The European Physical Journal C*, 63(4), sep 2009. doi: 10.1140/epjc/s10052-009-1133-9. URL https://doi.org/10.1140%2Fepjc%2Fs10052-009-1133-9.

[35] J. Putschke, K. Kauder, E. Khalaj, A. Angerami, S. Bass, S. Cao, J. Coleman, L. Cunqueiro, T. Dai, L. Du, et al. The JETSCAPE framework. *arXiv preprint arXiv:1903.07706*, 2019.

[36] J. Casalderrey-Solana, D. C. Gulhan, J. G. Milhano, D. Pablos, and K. Rajagopal. A Hybrid Strong/Weak Coupling Approach to Jet Quenching. *JHEP*, 10:019, 2014. doi: 10.1007/JHEP09(2015)175. [Erratum: JHEP 09, 175 (2015)].

[37] J. Casalderrey-Solana, J. G. Milhano, D. Pablos, K. Rajagopal, and X. Yao. Jet Wake from Linearized Hydrodynamics. *JHEP*, 05:230, 2021. doi: 10.1007/JHEP05(2021)230.

[38] A. V. Belitsky, S. Hohenegger, G. P. Korchemsky, E. Sokatchev, and A. Zhiboedov. Event shapes in n=4 super-yang-mills theory. 9 2013. doi: 10.1016/j.nuclphysb.2014.04.019. URL http://arxiv.org/abs/1309.1424http://dx.doi.org/10.1016/j.nuclphysb.2014.04.019.

[39] H. Chen, I. Moult, X. Zhang, and H. X. Zhu. Rethinking jets with energy correlators: Tracks, resummation and analytic continuation. 4 2020. doi: 10.1103/PhysRevD.102.054012. URL http://arxiv.org/abs/2004.11381http://dx.doi.org/10.1103/PhysRevD.102.054012.

[40] D. M. Hofman and J. Maldacena. Conformal collider physics: Energy and charge correlations. 3 2008. doi: 10.1088/1126-6708/2008/05/012. URL http://arxiv.org/abs/0803.1467http://dx.doi.org/10.1088/1126-6708/2008/05/012.

[41] S. Rychkov. EPFL lectures on conformal field theory in D≥ 3 dimensions. 1 2016. doi: 10.1007/978-3-319-43626-5. URL http://arxiv.org/abs/1601.05000http://dx.doi.org/10.1007/978-3-319-43626-5.

[42] H. Chen, I. Moult, and H. X. Zhu. Spinning gluons from the qcd light-ray ope. 3 2021. doi: 10.1007/JHEP08(2022)233. URL http://arxiv.org/abs/2104.00009http://dx.doi.org/10.1007/JHEP08(2022)233.

[43] C. Andres, F. Dominguez, R. K. Elayavalli, J. Holguin, C. Marquet, and I. Moult. Resolving the scales of the quark-gluon plasma with energy correlators. 2022. URL http://arxiv.org/abs/2209.11236.

[44] C. Andres, F. Dominguez, J. Holguin, C. Marquet, and I. Moult. A coherent view of the quark-gluon plasma from energy correlators. 3 2023. URL http://arxiv.org/abs/2303.03413.

[45] K. Lee, B. Meçaj, and I. Moult. Conformal colliders meet the LHC. pages 1–8, 2022. URL http://arxiv.org/abs/2205.03414.

[46] E. Craft, K. Lee, B. Meçaj, and I. Moult. Beautiful and charming energy correlators. pages 1–9, 2022. URL https://arxiv.org/abs/2210.09311v1.

[47] P. T. Komiske, I. Moult, J. Thaler, and H. X. Zhu. Analyzing n-point energy correlators inside jets with cms open data. pages 1–13, 2022. URL http://arxiv.org/abs/2201.07800.

[48] J. Brewer, J. G. Milhano, and J. Thaler. Sorting out quenched jets. 12 2018. doi: 10.1103/PhysRevLett.122.222301. URL http://arxiv.org/abs/1812.05111http://dx.doi.org/10.1103/PhysRevLett.122.222301.

[49] W. F. for ALICE Collaboration. First energy-energy correlators measurements for inclusive and heavy-flavour tagged jets with alice. URL https://indico.cern.ch/event/1139644/contributions/5541331/attachments/2709459/4704634/QM2023_wide_wenqing_main_Sep5.pdf.

[50] K. C. Zapp. Geometrical aspects of jet quenching in JEWEL. *Physics Letters B*, 735:157–163, jul 2014. doi: 10.1016/j.physletb.2014.06.020. URL https://doi.org/10.1016%2Fj.physletb.2014.06.020.

Appendix A

Constituent subtraction

For the constituent subtraction, we recall the formula 4-momentum of a particle in terms of its transverse momentum and mass:

$$p^{\mu} = ((m_T + p_T)\cosh(y), p_T\cos(\phi), p_T\sin(\phi), (m_T + p_T)\sinh(y)). \tag{A.1}$$

The method involves three steps, with the first being the creation of two lists, one comprising thermal particles, $\{p^{\mathrm{Th},i}\}$, and the other containing the jet's particles and recoils, $\{p^j\}$. Next, all possible pairings $(p^{\mathrm{Th},i}, p^j)$ are formed and ordered with respect to the pair-wise distances ΔR_{ij}. Finally, each pairing is iteratively processed by subtracting in the 4-momentum formula A.1 the smaller p_T from the larger one and also subtracting the quantity m_T from the larger while setting the smaller to 0 in both cases, i.e.

$$\begin{aligned} &\max(p_T^{\mathrm{Th},i}, p_T^j) \to \max(p_T^{\mathrm{Th},i}, p_T^j) - \min(p_T^{\mathrm{Th},i}, p_T^j), \\ &\min(p_T^{\mathrm{Th},i}, p_T^j) \to\ 0, \end{aligned} \tag{A.2}$$

$$\begin{aligned} &\max(m_T^{\mathrm{Th},i}, m_T^j) \to \max(m_T^{\mathrm{Th},i}, m_T^j) - \min(m_T^{\mathrm{Th},i}, m_T^j), \\ &\min(m_T^{\mathrm{Th},i}, m_T^j) \to\ 0. \end{aligned} \tag{A.3}$$

This iteration can be done until one reaches the end of the list, or in alternative one can define a cut-off distance such that the iteration stops once reached, in order to avoid subtractions of particles that are far away and unlikely to be correlated. When the iteration is over, the momenta with $p_T = 0$ are removed, and the remaining particles constitute the final subtracted ensamble. Subtraction can be made at the event level or jet level; the latter requires some extra care, and for our work we will have only performed subtractions at the event level.

Once the subtraction process is over, one should perform some tests in order to make sure that it was properly executed. Two common tests are the mass distribution, $(1/N)dN/dM$, and the R_{AA}, displayed in fig A.1.

Regarding the first test, it is expected for the mass distribution of the unsubtracted ensamble to be completely different from the vacuum, while the subtracted should be slightly shifted with respect to the vacuum. This is observed in Figure A.1a

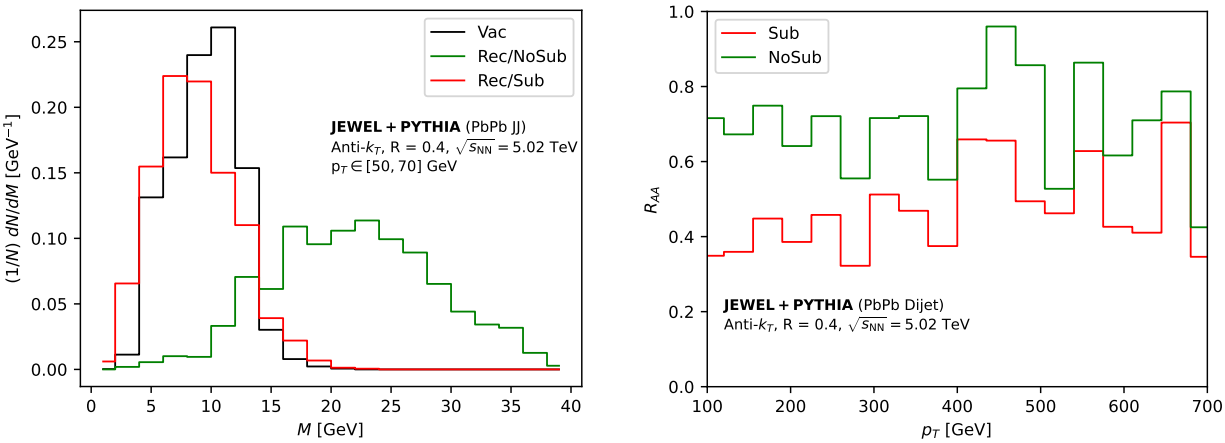

(a) Mass distribution

(b) R_{AA}

Figure A.1: **(left)** Mass distribution, for vacuum jets (black line), jets with recoils unsubtracted (green line) and jets with recoils subtracted. **(right)** R_{AA}, for jets with recoils unsubtracted (green line) and jets with recoils subtracted (red line).

On the other hand, the R_{AA} for the ubsubtracted event is expected to be substantially higher than it should, with the subtraction lowering it to common values of ~ 0.5, just like in Figure A.1b. If these tests are passed, it should be safe to assume that the subtraction has been correctly performed.